8-9-2006

Diluted Magnetic Semiconductor Nanomaterials Fabrication by a Chemical Vapor Deposition Method

Jingjing Liu
University of New Orleans

DILUTED MAGNETIC SEMICONDUCTOR NANOMATERIALS FABRICATION BY A CHEMICAL VAPOR DEPOSITION METHOD

A Thesis

Submitted to the Graduate Faculty of the
University of New Orleans
in partial fulfillment of the
requirements for the degree of

Master of Science
in
Applied Physics

by

Jingjing Liu

B.S. Southwest Jiaotong University, 1998
M.Eng. Southwest Jiaotong University, 2005

August 2006

ACKNOWLEDGMENT

This thesis and its experiments had gone through a special period of time in New Orleans: Hurricane Katrina. Therefore, there are a lot more than usual thankfulness that I would like to express.

Thank you to the faculty and staff at AMRI, UNO for providing me with the tools and facilities needed to complete this work. I want to acknowledge my advisor, Dr. Weilie Zhou, who gave me the opportunity to study and do research under DARPA grants (No. HR0011-04-1-0029), provided me with hands-on experience with SEM, TEM, and CVD devices, and taught me principles beyond school. A special thanks to Dr. Minghui Yu and Dr. Gabriel Caruntu who conducted SQUID and EPR experiments and share your fantastic ideals with me, which provides very important data and precious discussion to my thesis. Thank you to Dr. Gabriel Caruntu, Dr. Zhenjun Wang, and Dr. Paul Schilling for helping me with XRD analysis. Special thank you to Dr. Dongmei Cao in LSU Materials Characterization Center who provides us facilities including (SEM, TEM, and XPS) when ours were still recovering. And thanks to Dr. Kai Sun, Prof. Lumin Wang, and all the members in Lumin Wang's research group in University of Michigan, Ann Arbor who hosted me during the hurricane semester. I'll never forget the studying experience in UMich. Special thank you to all my colleagues, friends through graduate school in UNO, Jiajun Chen, Garrett May, Lesely Compbell Anglin, Huey, Cosmin Radu and Mo Zhu for every little help in the experiments, discussion of problems and encouragements through difficulties which carried me on through the past two years.

Thank you to Mary and George Lindquist, who hosted me when I was studying in Ann Arbor, Michigan. The warmth, strength and merriness when I was with you gave me memories that I will cherish and take with me when I move on with my life. Thank you to Lan Zhao, Jiangdong Li, Fang Wu, and Gekai for your help that led me through the one of my hardest time in the evacuation trip. Many thanks to all the people who gave me their hands during the Hurricane, I truly appreciate. Thank you to Mary Zervigon, Lisa McDondard, and Zhenzhen Mo, who provided me free accommodation before the university trailer ready. Without those help I couldn't imagine how I could pass the first two month in post Katrina New Orleans

Thank you to the many friends I have met at UNO. I will miss you. And finally, thank you to my mother and gradparents, Yingjia Liu, Yingqing Lu and Liangtian Yan, who have always been supportive throughout my life.

TABLE OF CONTENTS

Abstract vi

Chapter 1 Introduction 1

1.1 Diluted Magnetic Semiconductor 2

1.2 $Zn_{1-x}Mn_xO$ System 4

1.2.1 Crystal and Electronic Structures 5

1.3 CVD Methods 9

Chapter 2 Ferromagnetism Theory in DMS 11

2.1 Direct Exchange 12

2.2 Indirect Exchanges 13

2.2.1 *s*(*p*)-*d* Exchange Interactions 13

2.2.2 Super Exchange 15

2.2.3 Double Exchange 17

2.2.4 RKKY Interaction 18

2.25 Zener Model 19

Chapter 3 Experiment 21

3.1 Chemical Vapor Deposition System 21

3.2 Nanomaterials Fabrication 23

3.2.1 Approach I 23

3.2.2 Approach II 24

3.2.3 Approach III 26

3.3 Measurement 27

Chapter 4 Results and Discussion 29
4.1 Approach I 29
4.1.1 Morphology and Structure 29
4.1.2 Magnetic property 34
4.2 Approach II 36
4.2.1 Morphology 36
4.2.2 Structure Analysis 38
4.2.3 Magnetic property 42
4.3 Approach III 46
4.3.1 Morphology and Structure 46
4.3.1 Magnetic Property 52
Chapter 5 Conclusions 54
References 56
Vita 62

ABSTRACT

Well-aligned DMS $Zn_{1-x}Mn_xO$ nanowires and nanorods were successfully synthesized *in-situ* using a chemical vapor deposition method. Low-dimensional nanostructures such as bowls and cages were deposited on a silicon surface downstream of the tube furnace. Variation of reaction temperature and Mn doping level were investigated on structure and properties of the as-grown nanomaterials.

The as-grown nanowires and naorods are single crystalline wurtzite structure and possess a growth direction along the *c* axis. At 850 ºC, the most optimistic condition for ZnO crystal growth was obtained. At high reaction temperature 950ºC, Mn^{2+} were substitutionally doped into ZnO lattice, resulting in room-temperature ferromagnetic coupling with a saturated magnetization of 0.25emu/g. The ferromagnetic interaction is weakened, however, by larger concentration of Mn, due to the antiferromagnetic coupling of direct superexchange interaction between Mn^{2+}. The well-aligned DMS 1-dimensional Mn doped ZnO nanostructures have great potential for application in spintronic nanodevices.

CHAPTER 1

INTRODUCTION

The mass, charge, and spin of electrons in the solid state lay the foundation of the information technology we use today. Semiconductor devices generally take advantage of the charge of electrons, whereas magnetic materials are used for recording information involving electron spin.[1] If both the charge and spin of electrons can be used to further enhance the performance of devices, so called spintronics, we may then be able to use the capability of mass storage and processing of information at the same time, thus leading to a brand new era of information technology. Diluted magnetic semiconductors (DMS) in which the semiconductor cations are partially substituted by magnetic elements, is one of the important materials for the realization of spintronics. The ability to synthesize DMS 1-dimensional nanostructures could provide new building blocks for spintronics as well as open up new opportunities for fundamental physical studies. For this purpose, well-aligned $Zn_{1-x}Mn_xO$ nanowire/nanorod arrays were fabricated by a chemical vapor deposition method and their magnetic properties were studied in this thesis.

This thesis is organized as follows: In Chapter 1, the research background of DMS materials is introduced and the research objects are stated by answering several questions: why DMS is so important? Why do we choose $Zn_{1-x}Mn_xO$ as the designated chemical configuration? What's the advantage of one-dimensional nanostructures above films and

other morphologies? And why is CVD an effective method to fabricate DMS nanowires? In Chapter 2, the mechanisms of magnetic coupling will be discussed. In chapter 3, we will go through the CVD reactor set up, experimental procedures and characterization methods. The results will be discussed in Chapter 4, where the growth mechanism of the well-aligned nanowires and the origin of ferromagnetic interaction are proposed. The conclusion will be addressed in Chapter 5.

1.1 Diluted Magnetic Semiconductor

Magnetic semiconductors such as europium chalcogenides and semiconducting spinels that have a periodic array of magnetic elements (Figure 1(a))[1] were originally studied in the late 1960s to early 1970s. Unfortunately, the crystal structure of such magnetic semiconductors is quite different from that of conventional semiconductor Si and GaAs; in addition, the crystal growth of these compounds is notoriously difficult.

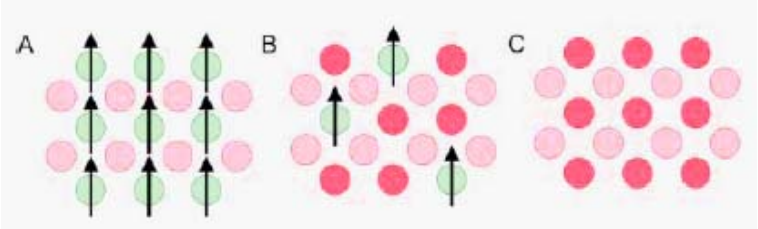

Figure 1.1 Three types of semiconductors: (a) a magnetic semiconductor, in which a periodic array of magnetic element is present; **(b**) a diluted magnetic semiconductor, an alloy between nonmagnetic semiconductor and magnetic element; and (c) a nonmagnetic semiconductor, which contains no magnetic ions.

Later on in 1979, a new category of semiconductor compound in which a fraction of the constituent ions is replaced by magnetic ions, so called the diluted magnetic

semiconductor (DMS) was first discovered by Galazka *et al*[2].

In contrast to magnetic semiconductors, DMS offer a possibility of studying the magnetic phenomena in crystals with a simple band structure and excellent magneto-optical and transport properties. Moreover, the well developed technology of growing these semiconductors allows for tuning their magnetic properties not only by an external magnetic field but by varying the band structure and/or carrier, impurity and magnetic ion concentrations.[3] The combination of spin degree of freedom and carrier electrons offers opportunities for a new generation of devices, which has the potential advantages of nonvolatility, increased data processing speed, decreased electric power consumption, and increased integration densities compared with conventional semiconductor devices[1]. However, ferromagnetic ordering above room-temperature, which has not been reported until recently[4], is critical for the application of spintronic devices such as spin-valve transistors, spin light-emitting diodes, and logic devices etc. Since the theoretical prediction of Curie temperature above 300K in transitional metal doped II-VI and III-V compound semiconductor by Delt [5], much effort has been done in both theoretical and experimental approach to realize room-temperature ferromagnetic ordering in such materials configuration. Ternary alloys of Zinc blend structure ZnS, ZnTe, CdS, HgSe etc. and wurtzite structure ZnO, GaN, GaAs doped with 3d transitional metal or rare earth elements Ti, V, Cr, Mn, Fe, Co, Ni were fabricated in the forms of bulk crystal, thin film, nanoparticles and one dimensional nanostructures. Fukumura *et al* [6]found a spin-glass behavior, Jung et al[7] observed ferromagnetic ordering with a T_c~45° C, Kane *et al*[8]

reported paramagnetic behavior at low temperature, and Tiwari *et al*[9] did not find any ferromagnetism above room temperature in both bulk and thin films of $Zn_{1-x}Mn_xO$ with x<4at. %. Meanwhile, magnetic interaction theories of DMS have been extensively studied. Several mechanisms were proposed and some of them are well-accepted. They are the s(p)-d(f) exchange interactions between orbits of host semiconductor and spins of magnetic atoms; superexchange, Blombergen-Rowland interaction, double exchange and the Ruderman Kittel Kasuya Yosida (RKKY) interaction between magnetic ions[3] etc.

1.2 $Zn_{1-x}Mn_xO$ System

Why do we choose $Zn_{1-x}Mn_xO$ composition? Among the family of possible transitional metal substituted DMS ternary alloys, $Zn_{1-x}Mn_xO$ has optimum chemical configuration for the following reasons. Firstly, the thermal solubility of isovalent Mn ion substation in ZnO is larger than 10 mol%[10], determined by ionic radius and valence states. Therefore large mount of Mn atoms can be introduced into ZnO lattice at thermal equilibrium condition though regular thermal evaporation or chemical vapor deposition (CVD) methods, characteristic of low cost than those non-equilibrium fabrication process such as pulsed laser deposition (PLD), molecular beam epitaxy (MBE) etc. Secondly, the electron effective mass of Mn is as large as ~0.3 m_e, where m_e is free-electron mass, which means the amount of injected spins and carriers can be large.[9] Thirdly, the substitution of Mn atoms in the ZnO lattice are also characterized by highly efficient electronluminescence, which make $Zn_{1-x}Mn_xO$ important in the context of optical flat

panel display application.[11]. ZnO is a well-known piezoelectric material for its anisotropic crystal structure and therefore incorporation of ferromagnetism in ZnO can lead to a variety of new multifunctional phenomena.

1.2.1 Crystal and Electronic Structures

The two crystal structures of Mn doped II-VI semiconductor, wurtzite and zinc blend, are very closely related, as shown in Figure 1.2, in spite of the difference in symmetry, in that they are both formed with tetrahedral (s-p^3) bonding, involving the two valence s electrons of the group II element and the six p electrons of the group VI element.

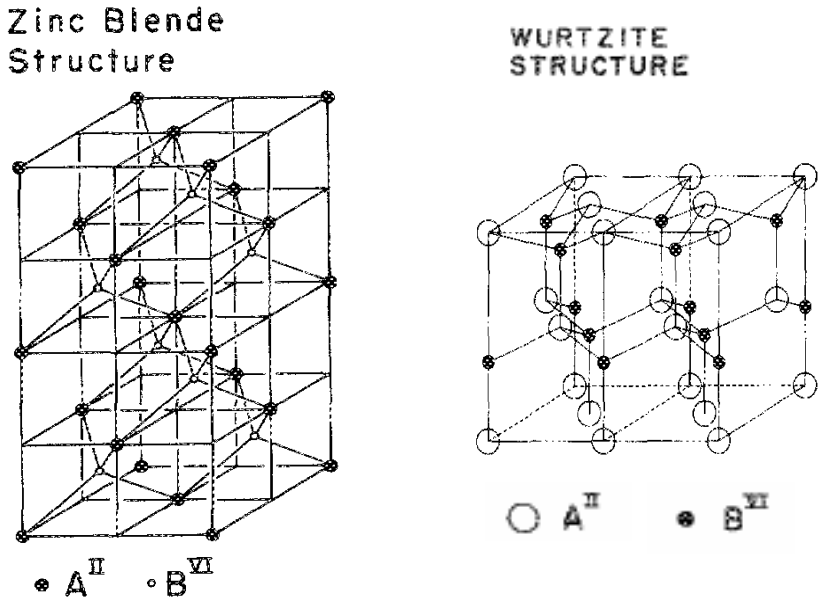

Figure 1.2 schematics of II-VI semicondutor compound. a) zinc blend structure b) wurtzite structure

Manganese is a transition metal with valence electrons corresponding to the $4s^2$ orbital. Although Mn differs from the group II elements by the fact that its *3d* shell is only half-filled, it can contribute its $4s^2$ electrons to the s-p^3 bonding as demonstrate in Figure 1.3,[12]

and can therefore substitutionally replace the group II elements in the tetrahedral structures.[11] The *3d* orbitals of Mn are exactly half-fill, according to Hund's rule all five spins are parallel in this orbital and it would require considerable energy (about 6-7 eV) to add an electron with opposite spin to the Mn atom. In this sense the Mn atom is thus more likely to resemble a group II element than other transition-metal elements.[13]

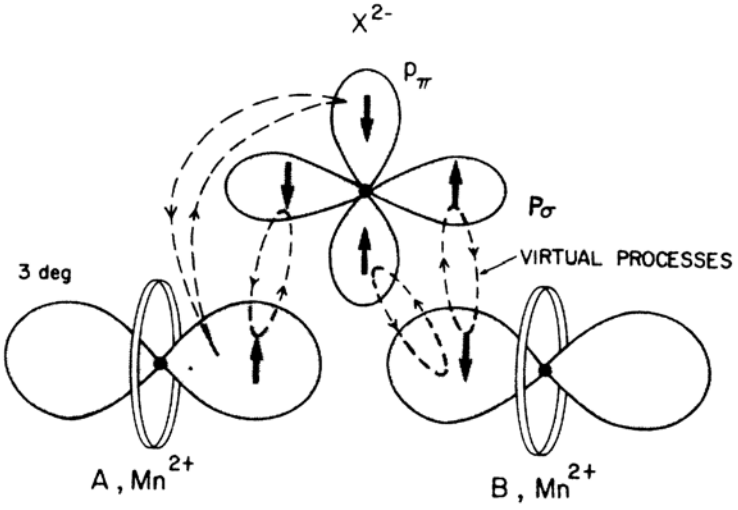

Figure 1.3 Schematic representation of the closest Mn^{2+}-O^{2}-Mn^{2+} configuration for both zinc-blende and wurtzite structures, where O^{2-} is the intervening anion. Both σ and π types of orbitals for p electrons are shown.

In principle, the properties of atoms, molecules and solids can be understood from their electronic structure calculated using quantum mechanics.[14] DMS is a disordered system, i.e., host atoms are randomly substituted by magnetic ions. If carrier dopants are introduced to control charge density, they also distribute randomly in the host material. Eventually, the DMS is a substitutionally disordered alloy. The band theory is constructed on the assumption of the periodic boundary condition, so disordered systems are out of the scope of band theory. One of the possible procedures to overcome this difficulty is to

arrange impurities regularly in the crystal neglecting the randomness. Owing to this arrangement, a large unit cell (super-cell) which contains impurity atoms is constructed. Then, the band structure calculation is performed for the super-cell.[14] To simulate randomness from first principles, coherent potential approximation (CPA) was further introduced to describe the DMSs by Sato *et al.* Their calculated density of states (DOS) for carrier doped $Zn_{1-x}Mn_xO$ are shown in Figure 1.4.[14] As shown in Figure 1.4(a), N-2*p* states hybridize well with Mn-3*d* states, because N-2*p* states are shallower than O-2*p* states. Due to this hybridization with the Mn-3*d* states, holes are itinerant with keeping their *d*-character, therefore the kinetic energy is lowered and the ferromagnetic state is stabilized. On the other hand, as shown in Figure 1.4(b), the doped electrons never go

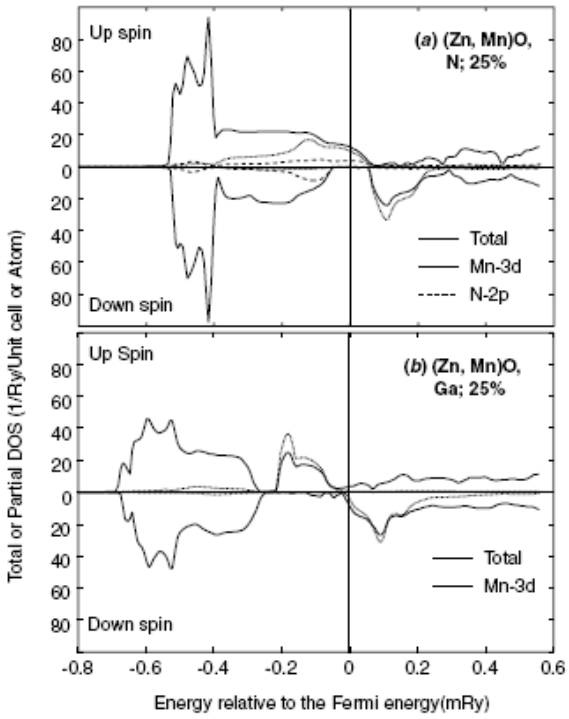

Figure 1.4 Total density of states per unit cell (solid line) and partial density of d-states per Mn atom at the Mn site (dotted line) in (*a*) 25% hole-doped and (*b*) 25% electron-doped cases in the ferromagnetic state. Mn atoms are doped up to 25%. In (*a*), the partial density of p-states per N atom at N site (dashed line) is also shown.

into the Mn-3d states but into the host conduction band, not stabilizing the ferromagnetism.[14]

The fivefold degenerate d-states of Mn impurity are split into doubly degenerate dγ-states and threefold degenerate dε-states in the tetrahedral coordination. Two dγ -states have the symmetries $3z^2$-r^2 and x^2-y^2. Three dε-states have the symmetries xy, yz and zx. The wave functions of these dε-states are extended to anions hybridizing well with O-2p states which make the host valence band, so that bonding states (t^b) and anti-bonding counterparts (t^a) are created as schematically shown in Figure 1.5.[14] On the other hand, the wave functions of the dγ-states are extended to the interstitial region, therefore, the hybridization of the dγ-states with the host valence band is weak and dγ -states remain as non-bonding states (e) as shown in Figure 1.5.

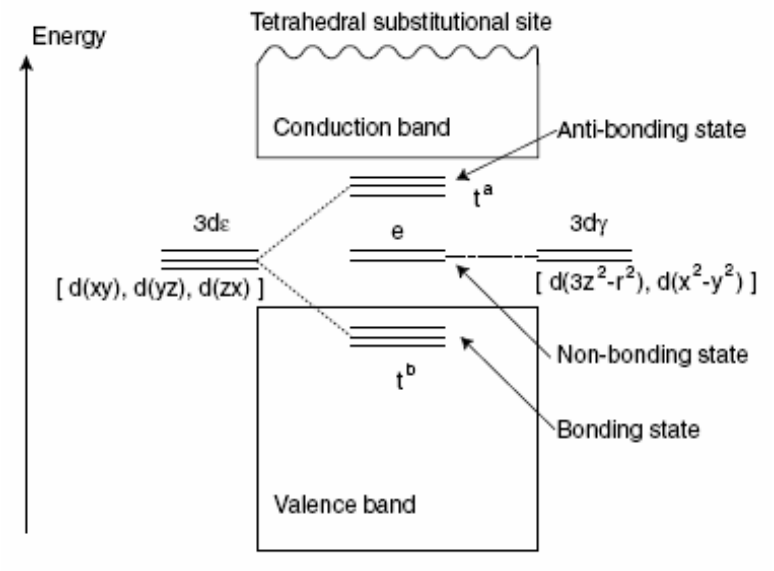

Figure 1.5 A schematic electronic structure of TM at the tetrahedral substitutional site. The anti-bonding t^a states and non-bonding e-states appear in the band gap.

1. 3 CVD Methods

By far, different fabrication process have been employed to synthesize $Zn_{1-x}Mn_xO$ epitaxial films, microcrystalline thin films, nanoparticles, nanowires resulting in various kind of magnetic properties. Non-equilibrium methods such as PLD, MBE are effective methods to grow DMS films at low temperatures. However, for nanowires growth, conditions are critical and barely repeatable. Moreover, large amount of defects such as vacancy, interstitials is unavoidable for non-equilibrium processes. Electron beam lithography with wet chemical etching techniques[15] and incorporation of the semiconductor alloy into the ordered wire-like pores of mesoporous silica hosts[16], metal organic chemical vapor deposition (MOCVD)[17] were employed to fabricate DMS nanowires. However, these approaches are rather time consuming and costly. DMS nanowires were synthesized by ion implantation after thermal evaporation by *Ronning et. al*.[18] But since dopant ions were introduced after the formation of nanowire, the distribution of Mn ions in ZnO matrix is inhomogeneous. To fabricate room-temperature ferromagnetic $Zn_{1-x}Mn_xO$ nanowires through a simple method is of great importance for both theoretical research of the physical basis and spintronics application. Chemical vapor deposition (CVD) is chemical reactions which transform gaseous molecules from precursors or start materials, into designated solid materials, e. i. thin film or nanostructures, on the surface of a substrate. Horizontal tube furnace CVD method has been widely used to synthesize a variety of nanowire materials. Since reactions are taking place by collisions of gaseous molecules of both matrix materials (ZnO) and dopants

(Mn), CVD methods are efficient in homogeneous doping. In the aspect of host materials, ZnO is easy to form one-dimensional nanostructures in thermal equilibrium conditions, because in wurtzite structure crystal tends to grow along c axis in order to maximize area of the lower energy {210} and {010} facets[19]. Combining the reasons above, CVD is a simple, time and cost efficient method to achieve one-dimensional nanostructure growth of $Zn_xM_{1-x}O$.

CHAPTOR 2

FERROMAGNETISM THEORY IN DMS

The understanding of the origin of the remarkable properties of DMS started with a model of their band structure[20], in which two electronic subsystems were distinguished: one containing delocalized, band electrons (described in terms of the virtual crystal approximation by extended states built from Bloch tight-binding functions) and the other consisting of the magnetic impurity electrons with magnetic moments localized in the ionic open 3d (or 4f) shell. The low energy dynamics of the mobile carriers, electrons in the conduction band and holes in the valence bands, is described by the effective mass theory. The tight-binding calculations for II-VI wide-gap semiconductors indicate that the conduction Γ_6 band Luttinger functions are mostly composed of cation *s* orbitals whereas Γ_8 and Γ_7 valence band functions mostly consist of anion *p* orbitals. Primarily these effective-mass carriers determine the electrical and optical properties of DMS crystals. On the other hand, the localized magnetic moments are responsible for the fact that DMS exhibit magnetic properties. In general, spin interactions are model descriptions of the spin-dependent part of Hamiltonian, which represents the low energy dynamics of the quantum many-electron system. The Hamiltonian describing the spin-dependent coupling between a band carrier and the localized magnetic moment is usually called the Kondo Hamiltonian, in which the last term represents the Coulomb interaction between the

localized and band electrons. On the other hand, the very similar Anderson Hamiltonian, widely used in many-body solid state physics can also lead to the spin-dependent exchange interaction. In the Anderson Hamiltonian the last term of is replaced by the so-called hybridization term neglected by Kondo, responsible for the mixing of band states with the localized state. The two independent exchange mechanisms, i.e. the hybridization-mediated kinetic exchange and the direct Coulomb exchange, are responsible for the spin-dependent interactions between band carriers and localized impurity magnetic moments in DMS.

2.1 Direct Exchange

The direct Coulomb exchange is a first-order perturbation effect:

$$\hat{H}_{ex} = -2\sum_{k,k'} J_{kk'} e^{i(\vec{k}'-\vec{k})\vec{R}_I} \hat{\vec{S}}L \cdot \hat{\vec{S}}_{kk'} \qquad (1)$$

Where $J_{kk'}$ is the exchange constant, $\hat{\vec{S}}L$ is the spin operator of the state L of the impurity at position R and, $\hat{\vec{S}}_{kk'}$ is the spin operator for band electron. The exchange constant is positive, i.e. it favors the parallel alignment of the band electron spin to the spin of the impurity. For the s-like conduction bands and for transition metal ions with the open d shell has shown that the direct Coulomb exchange always leads to a ferromagnetic Kondo Hamiltonian with the total spin of magnetic impurity S.[21] By summing up the thermodynamical averages of the spin multiplied by $e^{i(\vec{k}'-\vec{k})\vec{R}_I}$ over randomly distributed magnetic ions, one gets the carrier-ion direct exchange Hamiltonian for a Γ_6-band electron in the form:

$$H_{ex} = -xN_0\alpha\langle S_{//}\rangle s_{//} \qquad (2)$$

where $s_{//}$and $\langle S_{//}\rangle$ are the components along the magnetic field of the band electron spin and the thermodynamical average of the impurity spin, respectively; xN_0 is the concentration of magnetic ions and α denotes the exchange constant for s-like electrons. Most optical, transport and magnetic properties of the band electrons in DMS were successfully interpreted within the virtual crystal and mean field approximations.

2.2 Indirect Exchange

2.2.1 *s*(*p*)-*d* Exchange Interactions

Schrieffer and Wolf proved [22, 23] that the hybridization terms in the Anderson Hamiltonian also led to the Kondo Hamiltonian involving the total spin of the impurity, but with opposite sign of the exchange constant. Dietl and Bhattacharjee *et al*[24] suggest that the hybridization-mediated p-d kinetic exchange is responsible for the observed sign and magnitude of the constant in Mn-based II-VI DMS. Within the *k*-space perturbational approach, the p-d hybridization can be described in terms of virtual transitions of an electron between p bands and the ionic d shell. The singly occupied orbital of Mn^{2+} ion can participate in the virtual transitions involving both the creation and the annihilation of a band electron (as shown schematically in Figure 2.1[3]). The spin dependence of the hybridization-induced interactions results from the Pauli principle, which allows only for virtual transitions decreasing the total spin of the ion (either by removing the electron spin from the d orbital or by adding one with opposite spin). This leads to an antiferromagnetic, Kondo-like interaction. For an empty (or doubly occupied) orbital the

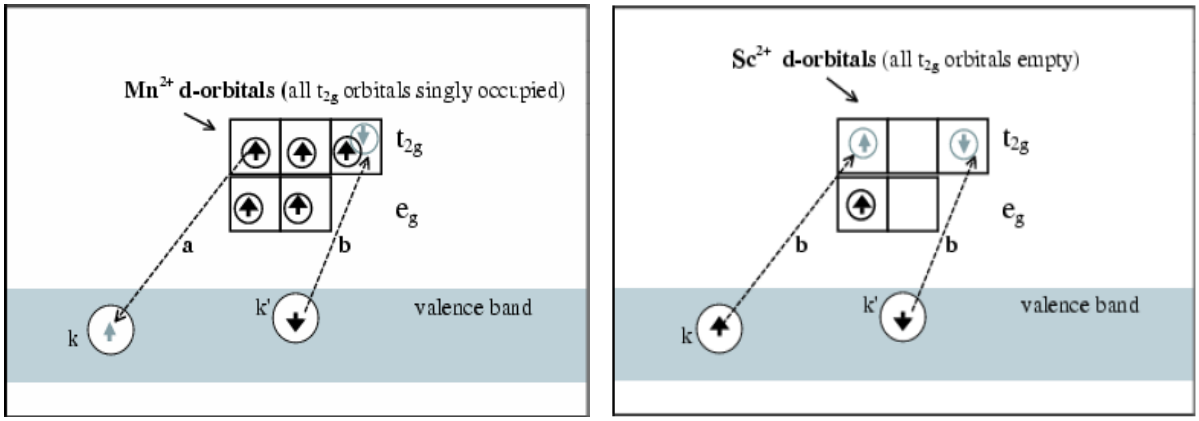

Figure 2.1 (a) For a singly occupied d orbital (like Mn^{2+}) both kinds of virtual transitions, i.e. the transfer of an electron from the ion to the valence band '*a'* and from the band onto the ionic d shell '*b*', decrease the total spin of the ion, due to the Pauli principle. For an empty d orbital (like all *t2g* orbitals in Sc2+ or Ti2+) only the virtual transitions (*b*) from the valence band into the ion are possible--a band electron with spin up as well as an electron with spin down can be transferred. According to the Hund rule, the transition which increases the total spin of the ion leads to lower energy.

Pauli principle does not favour any direction of electron spin (Figure 2.1(b)). Still, the interaction remains spin dependent as the ion prefers to increase its total spin, according to Hund's rule. The spin-dependent part of the effective Hamiltonian obtained for the interaction between a Γ_8 electron and an impurity with all t_{2g} d orbitals occupied by one electron has the Kondo-like form:

$$\hat{H}_{ex} = -\frac{1}{3} x N_0 \beta_N \langle S_{//} \rangle J_{//} \qquad (3)$$

where $J_{//}$ is the component of the fictitious total angular momentum of Γ_8 valence-band electron along the external magnetic field. The exchange constant β_N is negative for Mn^{2+}, i.e. leading to the antiferromagnetic interaction, determined by that all d orbitals hybridize with the Γ_8-band states (t_{2g}) singly occupied.

These results lean heavily on the particular symmetry of both the crystal potential

acting on the paramagnetic ion and of the valence band states--they are subjected to considerable change when different symmetries are considered. In II-VI DMS with a wurtzite structure the axial anisotropy of the kinetic exchange interaction has been observed in $Cd_{1-x}Mn_xSe$ [25] and $Cd_{1-x}Co_xSe$ [26] $Zn_{1-x}Mn_xO$ [27], was shown to result from the anisotropy of the hybridization matrix elements[28].

2.2.2 Superexchange

When looking for DMS with desired magnetic properties, e.g. ferromagnetism, we have to study the interactions that couple the spins of magnetic ions. There are several microscopic mechanisms that lead to the spin-spin (d-d) interactions between two magnetic ions. Four main mechanisms leading to spin-spin interactions are presented in this section in the form in which they were invoked to explain the interactions between magnetic ions in DMS. In two of them, i.e. in the super exchange and the double exchange, within the standard atomic picture, the interaction can be thought of in terms of a virtual transition between the ions and neighboring anions. While in the two other mechanisms, the s(p)-d exchange was shown to lead either to the polarization of the free electron gas (Ruderman-Kittel-Kasuya-Yoshida (RKKY) mechanism) or to the inter-band polarization (Blombergen-Rowland interactions) and the spin-spin interactions resulted from this polarization.

Larson *et al*[29, 30] showed that for II-VI DMS the superexchange, resulting from the sp-d hybridization, is by far the dominant spin-spin interaction responsible for the observed isotropic (Heisenberg) and anisotropic (DM) exchange constants. The superexchange is a

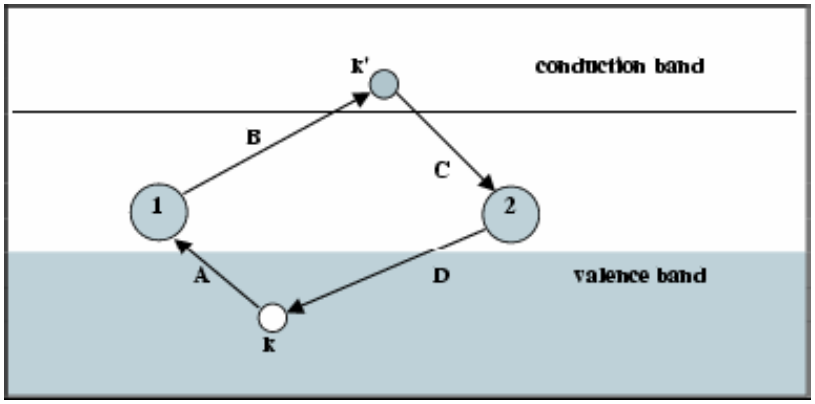

Figure 2.2 Schematic illustration of the four virtual transitions leading to the superexchange ion-ion interactions. The arrows show the directions in which the electrons are transferred for the path ABCD--for the path CADB, for example, all the directions would be reversed.

process in which the spins of two ions are correlated due to the spin-dependent kinetic exchange interaction between each of the two ions and the valence p band. Using the virtual transition picture, one can say that the superexchange is a result of four virtual transitions (from the band onto the ions and back to the band--as shown in Figure 2.2, by the lines A, B, C and D). This can be done in six sequences: ABCD, ABDC, BACD, BADC, ACBD and CADB, which all start with the transfer of the band electron k onto one of the ions (i.e. producing a hole in the band) but lead to different intermediate states in the perturbation Hamiltonian matrix. The unperturbed valence band states, which have to be summed up over the entire Brillouin zone, are usually described within the empirical tight-binding model. to determine the fourth-order perturbation matrix for the hybridization Hamiltonian, one has to properly select intermediate states $|n\rangle$ and $|n'\rangle$ correspond to one ion with N electrons and the second with N+1 electrons and one hole in the p band (one band electron is transferred to the ionic d shell) whereas the $|l\rangle$ states

may be of two types, either N+1 electrons on both ions and two holes in the band (for the paths ABCD, ABDC, BACD and BADC in Figure 2.2) or no holes and one ion with *N*+1 and the other with *N*-1 electrons (for ACBD and CADB in Figure 2.2). For Mn^{2+} of which all hybridizing d orbitals (t_{2g}) are singly occupied, the superexchange for both nearest-neighbour (NN) and next-nearest-neighbour (NNN) interaction is antiferromagnetic--the Heisenberg exchange constant J obtained is inversely proportional to S^2.

2.2.3 Double Exchange

The mechanism of spin-dependent interaction between magnetic ions in DMS considered in this section, the double exchange mechanism, was proposed nearly 50 years ago by Zener[32]. The double exchange couples magnetic ions in different charge states by virtual hopping of the `extra' electron from one ion to the other. Hasegawa *et al*[33] considered an Mn^{2+}-Mn^{3+} pair of ions with one d electron hopping virtually from one ion to the other via the p orbitals of neighboring anions. Recently, the coexistence of Mn2+and Mn3+ ions leading to double exchange was also suggested in ZnO[34] and the chalcopyrite semiconductor $CdGeP_2$[35]. A model d^4-d^5 pair of ions (Mn^{2+}-Mn^{3+}) in a semiconductor zinc-blende crystal was considered resulting from the complete degeneracy of the states $1d^42d^5$ and $1d^52d^4$ by Blinowski *et al*[36], in which both the double exchange and the superexchange may be effective. Instead of localized anion levels, band state was considered the virtual electronic states in semiconductor. The hopping operators

transfer the electron with the spin σ from the lth d orbital of the ion *j* to the same orbital of the ion *i*. The double exchange term has a non-Heisenberg character and, favours large values of S, i.e. the ferromagnetic alignment of the ionic spins.

2.2.4 RKKY Interaction

As all the mechanisms described above, the spin-dependent exchange coupling between the ionic and band states plays a crucial role in the RKKY mechanism. What makes RKKY really different is that, in contrast to the other mechanisms, it becomes efficient only when a high concentration of free carriers is present. The basic idea of RKKY is very simple: the ions interact with the band electrons due to the Coulomb exchange described by the s-d Kondo Hamiltonian, resulting from the second-order perturbation. The energy of the exchange coupling depends on the density of states of the mobile carriers at the Fermi level and on the exchange integral of the s-d interaction. Thus, the RKKY interaction is ferromagnetic at short distances and, at larger distances, oscillates with decreasing amplitude. When the Fermi level entered the band of heavy holes and these holes could contribute to the RKKY mechanism, the concentration-induced paramagnet ferromagnet transition was observed. The observed breakdown of the long-range ferromagnetic order and the formation of a spin-glass state for the carrier concentrations above $p = 10^{21}$ cm^{-3} was explained by the oscillatory character of the RKKY interaction.[37, 38] Knowing the dependence of exchange coupling energy on the distance between the spins one can calculate the mean-field value of their Curie-Weiss temperature. Dietl's[39, 40] quantitative calculation doesn't have positive view of

ferromagnetism in II-VI DMS, while on the other hand, Kacman[3] suggest that the ferromagnetic coupling between Mn spins is driven by weakly localized holes, whose states can be regarded as extended.

2.2.5 Zener Model

Recently, it was shown by Dietl *et al*[5, 41] that in the limit of carrier densities lower than in metals, i.e. when the mean ion-ion distance is small with respect to $1/k_F$, the Zener model has to be invoked to explain the observed properties of Mn-based III-V and II-VI thin films and heterostructures. This is due to the importance of the k-p, spin-orbit and carrier-carrier interactions, which are difficult to take into account within the RKKY

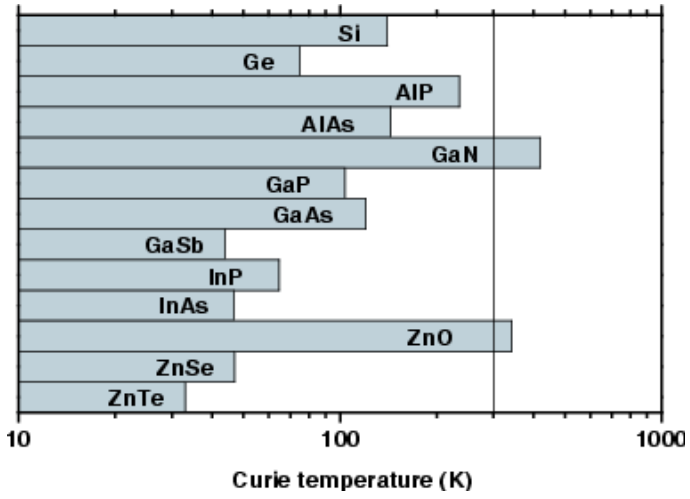

Figure 2.3 Computed values of the Curie temperature *T*C for various p-type semiconductors containing 5% of Mn and 3.5×10^{20} holes per cm^3.

model. Zener put forward a model of ferromagnetic interactions mediated by free carriers in tetrahedrally coordinated semiconductors, in which the spin polarization of the localized spins results in a spin splitting of the bands and that in this situation the

exchange coupling between the carriers and the localized spins leads to ferromagnetism. Since the carriers in the studied systems are at the localization boundary, Dietl *et al*[5] suggest that the holes in the extended or weakly localized states mediate the long-range interactions between the localized spins on both sides of the Anderson-Mott metal-insulator transition (MIT). The model implies that the Curie temperature is determined by a competition between the ferromagnetic and antiferromagnetic interaction. The authors computed the values of T_c for vavious semiconductors containing 5% of Mn and 3.5×10^{20} holes per cm^3 are presented (Figure 2.4). The data demonstrate there is much room for a furher increase of T_c in p-type DMS, thus intrigued the extensive studies in Mn, Co doped ZnO and GaN semiconductors.

CHAPTER 3

EXPERIMENT

3.1 Chemical Vapor Deposition System

Chemical vapor deposition (CVD) is chemical reactions which transform gaseous molecules from precursors or start materials, into designated solid materials, e. i. thin film or nanostructures, on the surface of a substrate. The process is widely used to fabricate a variety of nanowire materials. A CVD reactor is generally composed of a source of gases or vapors, control system of flowing gas, a reaction chamber, heating system, a vacuum pump for reduced-pressure operation, and treatment of the exhaust gases. Figure 3.1 shows a schematic of our horizontal tube furnace CVD system. The

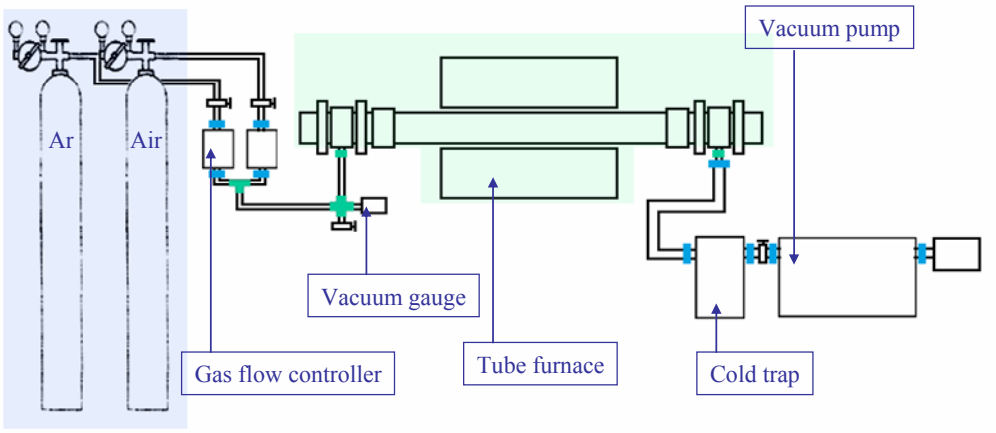

Figure 3.1 a schematic of the horizontal tube furnace CVD system used for $Zn_xMn_{1-x}O$ nanowires fabrication

components and their functions are listed in Table 3.1. Figure 3.2 shows a picture of the actual CVD reactor assembled for this project. Inside the heating area is the most

Table 3.1 Horizontal tube furnace CVD components

Component	Parts	Vender	Model #	Function
1. Gas feeding system	Mass flow controller	MKS	1179A22CR18K	Provide accurately control the multiple reactant gas flow rate
	4 channel read out	MKS	2470	
2. Heating system	1” Tube funace	Lindberg/Blue M	TF55035A-1	Provide temperature control
3. Reaction Chamber	1” quartz tube	QSI Quartz Scientific	QT022C	Where reactions take place
4. Vacuum system	Vacuum pump	LEYBOLD	91255-1	Provide desired ambiguous pressure inside chamber
	Needle valve	MDC	310072	
	Vacuum gauge	Vacuum Research	902056	
	connections	Swagelok; A&N; MDC	-	
5.Exhaust treatment	Cold trap	LEYBOLD	18820	Condensate the exhausts
	Smoke elimilator	LEYBOLD	99171125	Filtration of exhaust gases

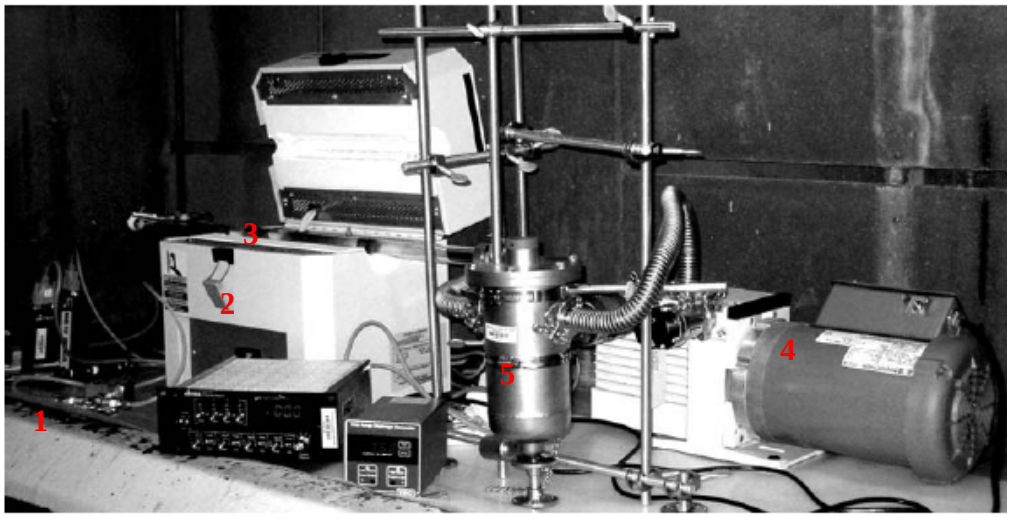

Figure 3.2 A picture of the assembled tube furnace CVD system. Number 1-5 denote the parts described in Table 3.1.

critical part of the CVD reaction system, where the start materials are placed at the center of furnace and (001) Silicon substrate is positioned at the down stream end of the furnace (illustrated in Figure 3.3). Since substrate lays closed to the edge of heating area, there

exists a temperature gradient along the Si substrate, which was measured by standard K-type thermal couple.

3.2 Nanomaterials Fabrication

3.2.1 Approach I

Synthesis of DMS Mn doped ZnO nanowires was first reported by Chang *et al* [42] by simple vapor growth using pure Zn and $MnCl_2$ powder mixture as start materials. Nanowires with low-temperature ferromagnetism were fabricated on the Si substrate downstream after 160 minutes of reaction at 500ºC under argon flow of 100 sccm (standard cubic centimeter per minute) at vacuum pressure of 0.05mPa. The parameters and procedures of our first approach were designed to try to repeat this result. 99.9% Zn powder (Alfa Aesar) and 99% $MnCl_2 \cdot 6H_2O$ powder (Alfa Aesar) were mixed with atomic

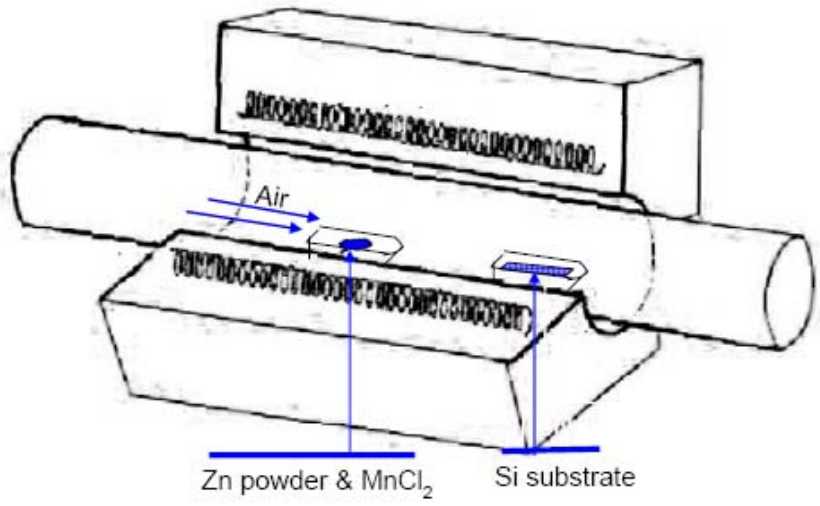

Figure 3.3 start materials and substrate layout inside tube furnace for approach I

ratio of 10:1 and put in a ceramic combustion boat sliding into the center of 1-inch quartz tube furnace. (100) Si substrate was placed at downstream side of quartz tube with a distance of 150 mm to the heating center and 15 mm away from the edge of furnace, as shown in configuration schematics of Figure 3.3. A temperature gradient was created in the deposition zone, which was calibrated by a standard K-type thermal couple. The mixture was then heated to 600 ºC and last for 4 hours under 50 sccm air flow at pressure of 8 Torr. No catalyst was used during the whole synthesis process. After the reaction, yellowish powder was generated *in situ* at the tube furnace center, and a deposition layer with light yellow color was grown on the Si substrate downstream, where the temperatures of the two regions were measured as 600 °C and 450–550 °C, respectively. Sample name are labeled in Table 3.2. Residue of gray Zn power was also observed *in situ*.

Table 3.2 Sample names and corresponding reaction condition in approach I

Sample name	Temperature (ºC)	Time (min.)	Products position	Norminal Mn atomic ratio (at.%)	Pressure (Torr)	Gas type/flow rate (sccm)
6-I	600		*in situ*			
6-S1	~550	160	Si substrate	10	8	Ar/100
6-S2	~450		Si substrate			

3.2.2 Approach II

In order to pursue a complete reaction of the Zn, we changed a variety of reaction conditions. The reactor configuration is shown in Figure 3.4. Zn foil (99.9 % purity Alfa Aesar) was employed as the zinc source of the start materials in order to achieve higher surface contact between zinc and oxygen in the ambient environment. $MnCl_2 \cdot 6H_2O$ was

still used to provide the manganese source in the system. Higher temperature and shorter heating duration were set in the CVD reaction. The synthesizing temperature variation was performed to study its influence on the morphology, composition and magnetic properties of the low dimensional nanomaterials. Start materials of high purity Zn foil and $MnCl_2 \cdot 6H_2O$ powder with atomic ratio of Zn:Mn=10:1 were placed in ceramic boat and loaded at the center of a 1-inch diameter quartz tube furnace. The reaction was conducted at 750ºC, 850ºC and 950ºC for 30minutes respectively. Sequentially designated gases were introduced into the reaction chamber at the melting point of metallic zinc to induce ZnO nanowire growth. Argon at a flow rate of 25 sccm was used to protect Zn foil from reaction before temperature reach the melting point 420ºC. After

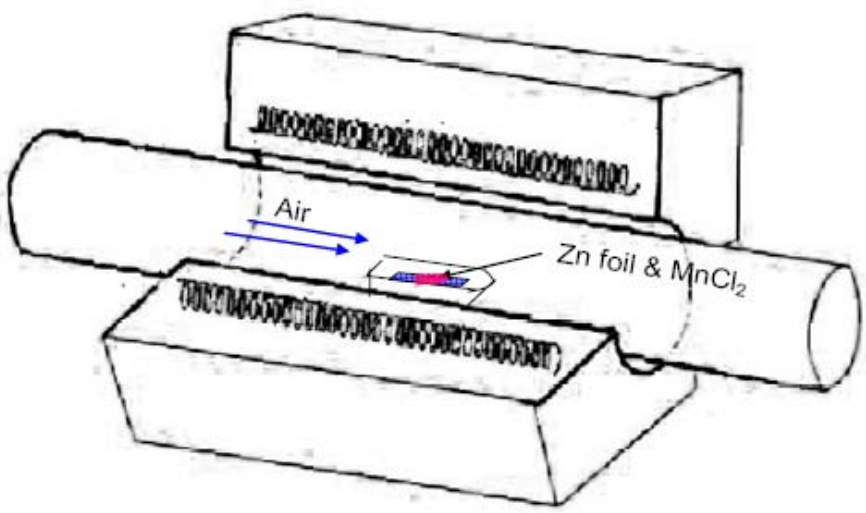

Figure 3.4 schematic of reactor configuration for approach II

that, air at a flow rate of 50sccm was switched into the quartz tube. Simultaneously, Zn/ZnO droplets were formed on the surface of the Zn foil providing a seeding layer of

nanowire growth. At the end of the reaction processes at different temperature, yellowish flakes were obtained at the location where the Zn foil was placed. No residual Zn foil was found after the reaction. The samples of each reaction were labeled in Table 3.3.

Table 3.3 Sample names and corresponding reaction condition with temperature variation in approach II

Sample name	Temperature (ºC)	Time (min.)	Products position	Norminal Mn atomic ratio (at.%)	Pressure (Torr)	Gas type/flow rate (sccm)
7-3-I	750					
8-3-I	850	30	in situ	10	8	Air/50
9-3-I	950					

3.2.1 Approach III

Change of Manganese concentration in $Zn_{1-x}Mn_xO$ system was studied in this approach. The configuration inside the reactor was slightly changed. Zn foil was placed perpendicular to the gas flow direction as illustrated in Figure 3.5. Similar fabrication process was taken except for the quantity of $MnCl_2 \cdot 6H_2O$ added to reach nominal doping ratio was set at 5 at. %, 10 at.%, and 15 at. %, respectively. No residual Zn foil was found

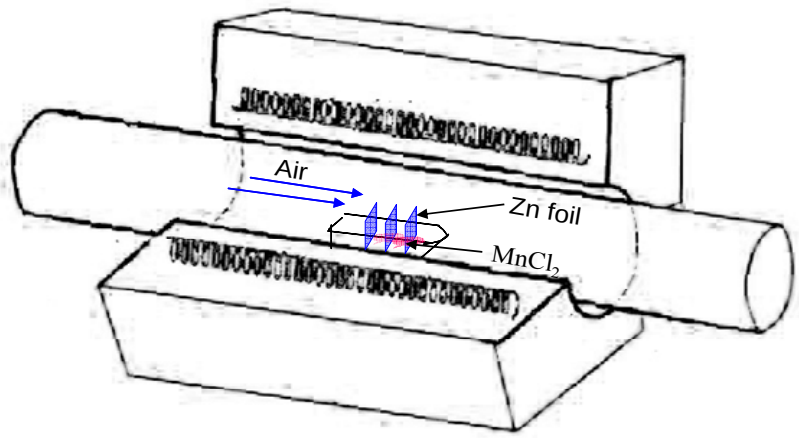

Figure 3.5 schematic of reactor configuration for approach II

at the end of each reaction. Yellowish flakes of gradually thicker color were obtained *in situ* for each reaction as the doping percentage of Mn increasing. Samples were named after the change of Mn concentration (Table 3.4).

Table 3.4 Sample names and corresponding reaction condition with temperature variation in approach II

Sample name	Norminal Mn atomic ratio (at.%)	Temperature (ºC)	Products position	Reaction time (min.)	Pressure (Torr)	Gas type/flow rate (sccm)
8-3-IA	5					
8-3-IB	10	850	in situ	30	8	Air/50
8-3-IC	15					

3.3 Measurement

Carl Zeiss 1530 VP field-emission scanning electron microscope (FESEM) was used to reveal the morphologies of the as-obtained materials from the three approaches described in the above section. Energy dispersive x-ray analysis (EDAX) by a energy dispersive x-ray spectrometer (EDS) equipped inside the FESEM was conducted to investigated the chemical composition of materials. The crystal structure of the as-prepared nanomaterials was investigated by a JEOL 2010 transmission electron microscope (TEM) at 200 kV. Selected area diffraction pattern (SADP) and lattice fringe images of were obtained to further determined the structure and defects inside the Mn doped ZnO nanowires. Philips X'Pert-MPD x-ray diffractometer (XRD) was also employed to probe the phase composition and crystal lattice features of the fabricated nanostructures. The X-ray scan was conducted under CuKα (λ=1.54056Å) radiation at a scan rate of 0.05° 2θ steps per second from 20° to 90°. The magnetic properties of the as-

synthesized nanowires were investigated by an MPMS-5S superconducting quantum interference device magnetometer (SQUID). Magnetization as a function of applied magnetic field at 5K and 300K as well as the magnetization as a function of temperature curves were obtained by SQUID. EMX Bruker Electron paramagnetic resonance (EPR) spectrometer was used to measure the ferromagnetic resonance sprectrum (FMR) of the as synthesized materials at 9.88GHz X band. X-ray photoelectron spectroscopy (XPS) was conducted on a QRATOS: Axeis 165 XPS spectrometer at 10 mA and 15 kV anode HT using mono Al as the reference.

CHAPTER 4

RESULTS AND DISCUSSION

4.1 Approach I

4.1.1 Morphology and structure

Figure 4.1 shows nanorods fabricated *in situ* of quartz tube center at 600 °C (Sample 6-I). The as-synthesized nanorods are about 200 nm in diameter and 15 μm in length. No hexagonal facets was observed in the enlarged FESEM image of the nanorods (Figure 4.1(b)). Nanostructures with distinct morphology were obtained at different temperature zone on Si substrate at the downstream end of the tube furnace. Figure 4.2 demonstrated nanostructured bowl and cage features deposited on the Si substrate for sample 6-S1 and

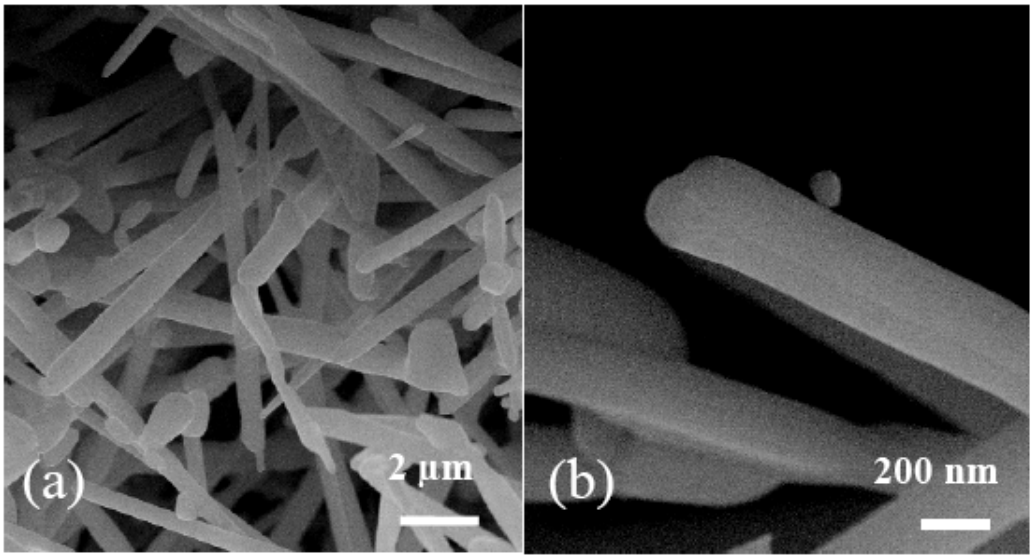

Figure 4.1 FESEM images of sample 6-I

6-S2 respectively. The bowls, ranging from 4 to 6 μm in diameter and consisting of 80 nm nanocrystals, were obtained at the temperature zone of 500-550 °C, as shown in Figure 4.2(a) and (b). Cages with smaller diameter of about 2 μm, but consisting of larger

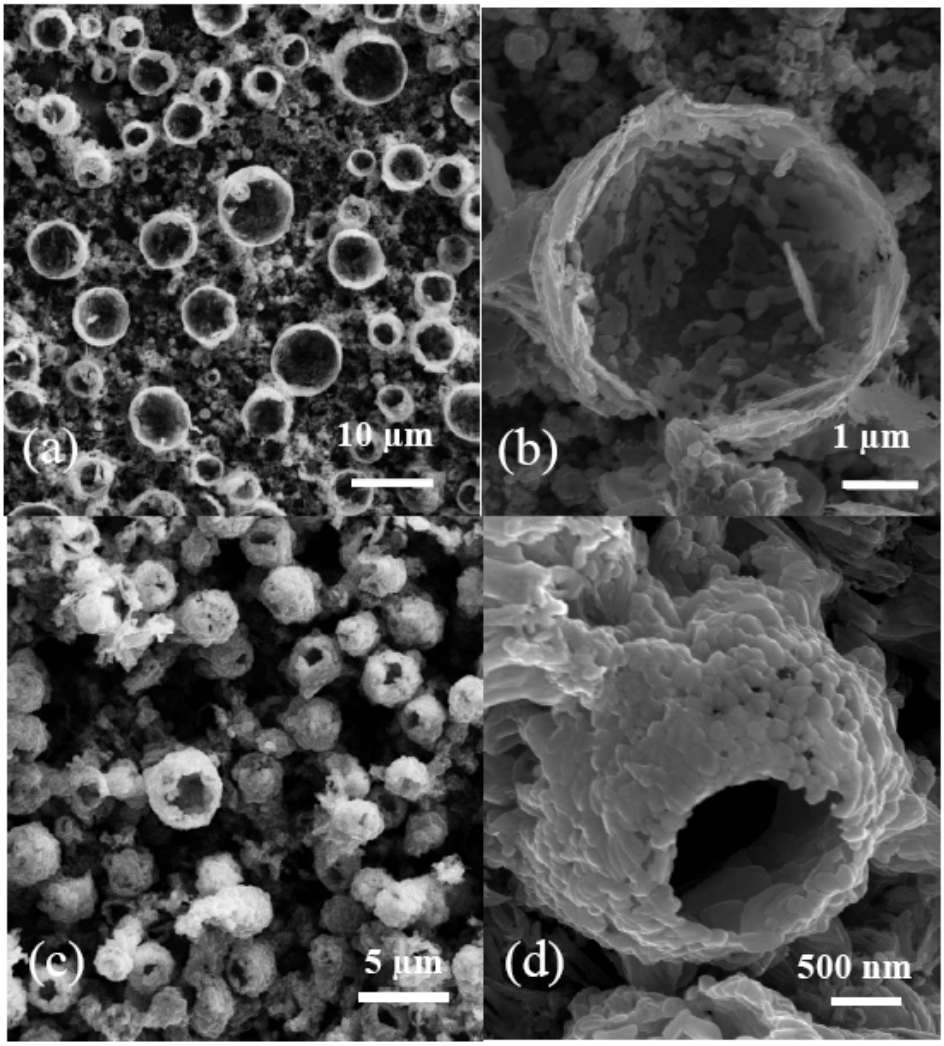

Figure 4.2 FESEM images of sample 6-S1 and 6-S2 obtained on Si substrate at different temperature zones of 600, 500–550, and 400–450 °C, showing nanocrystalline bowls and cages, respectively.

nanocrystals of 200 nm, were achieved at the lower temperature range of 400-450 °C (Figure 4.2 (c) and (d)).

Figure 4.3 shows a typical EDS spectrum of the as-synthesized nanorods. Zn and O peaks as well as Mn peaks were observed, indicating successful Mn doping in ZnO. The estimated Mn atomic ratio in ZnO nanorods is around 2 at.%, and even lower in bowl and cage structures, much less than the nominal doping ratio, 10 at. %, which might be caused by the sublimation of Mn loss and synthesis conditions.[43] Figure 4.4 (a) shows the XRD pattern of the Mn-doped ZnO nanorods. In addition to the peaks representing pure ZnO powder, no extra peak was observed, which implies no existence of a second phase, such as manganese oxides or manganese composites which might give rise to the magnetic properties. Similar XRD results were obtained on bowls and cages as shown in figure 4.4 (b). Except for peaks correspond to Si substrate, only diffraction for pure ZnO was detected. Figure 4.5 is a TEM image of the as-grown nanorod, in which the inset is a corresponding selected area diffraction pattern (SADP), indicating the *c*-axis growth of

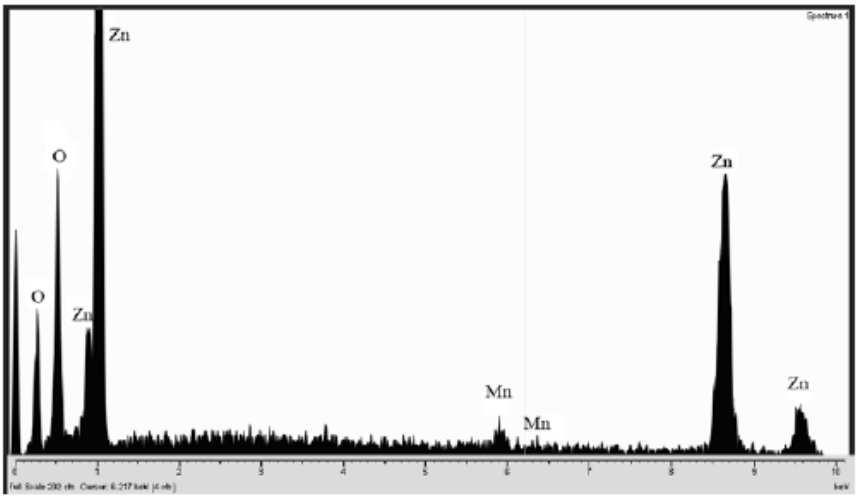

Figure 4.3 EDX spectrum of Mn doped ZnO nanorod.

the Mn-doped ZnO nanorods. Most nanorods were straight in shape and smooth in surface, consistent with the FESEM results. The as-grown bowl and cage structures are composed of polycrystalline ZnO nanocrystals, which were confirmed by diffraction rings of SADPs.

Recently, 1D ZnO nanostrustures have been intensively studied and vapor-liquid-solid (VLS), vapor-solid (VS) mechanisms are well accepted.[44, 45] In our experiment, nanorods were obtained as expected at 600 °C since ZnO nanocrystals tend to form one-dimensional structures along the *c* axis.[19] However, nanocrystalline ZnO bowls and cages were deposited at lower temperature zones. Although self-assembled ZnO spherical morphologies were observed,[46] ZnO nanocrystalline bowls and cages obtained in our experiment were seldom reported before. In our case, we suggest that the evaporated Zn atoms are carried to lower temperature downstream, when the concentration of Zn vapor meets certain value under the ambient condition, Zn atoms starts to condense on the Si substrate and incubated to micrometer scale, then by oxidization of the surface of Zn core, ZnO nanocrystals were grown out partially covering the Zn particles. With prolonging time, the Zn cores were sublimed, leaving the bowl and cage structures on the Si substrate. The feasibility of this mechanism were also reported by the observation of Sun *et al.*[47] and Kong *et al.*[48] of epitaxial growth of ZnO layers on Zn surface with rotation angles relative to the lattice of Zn core for the core-shell ZnO nanostructures and ZnO nanotubes. In our synthesis, at a higher deposition temperature zone of 500–550 °C, a larger Zn core was formed and sublimed faster before the oxidation layer had grown,

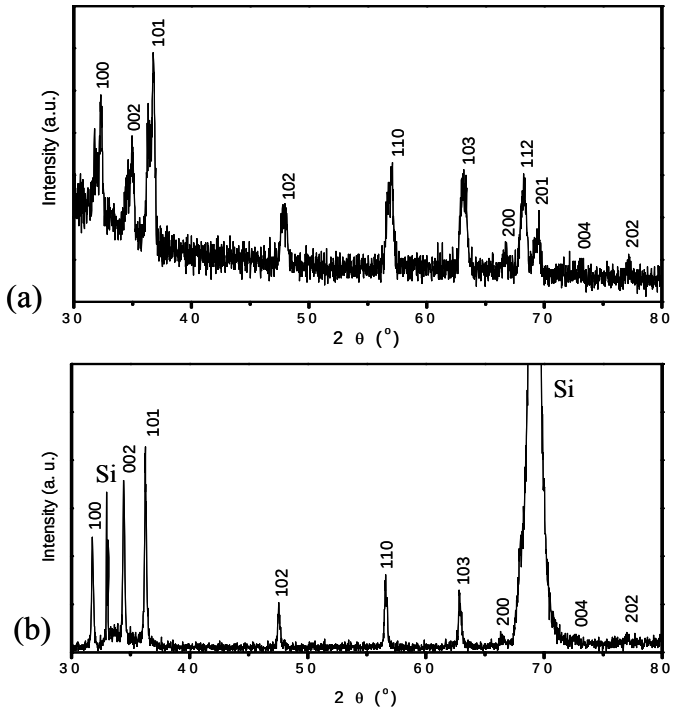

Figure 4.4 XRD patterns of (a) $Zn_{9.98}Mn_{0.02}O$ nanorods (b) Mn doped ZnO

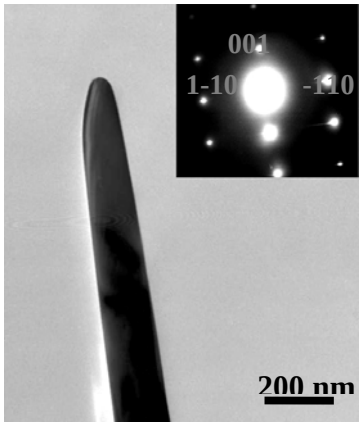

Figure 4.5 TEM image of a single $Zn_{9.98}Mn_{0.02}O$ nanorod. Inset is the corresponding SADP.

thicker, leading to bowl-like structures, while at the relatively lower temperature zone of 400–450 °C, the Zn core had smaller dimension and the ZnO nanocrystals had a longer growing period before the core had sublimed, resulting in cage like structures with

thicker edges. The evaporation pressure of Zn and ZnO as well as the partial pressure of the reactant elements are crucial influence factors to the condensation and sublimation of Zn core and the formation of ZnO nanocrystals, which need further studies.

4.1.2 Magnetic Property

The magnetization as a function of applied magnetic field for the as-prepared Mn-doped ZnO nanostructures were measured by SQUID magnetometer. The hysteresis loop of the as-synthesized $Zn_{9.98}Mn_{0.02}O$ nanorods exhibited an obvious ferromagnetic ordering at 5 K, as shown in Figure 4.6 (a). The estimated saturation magnetization per Mn ion and the coercivity field *Hc* for the nanorods are $1.1\mu_B$ and 138 Oe, respectively. The inset shows the temperature dependence of the magnetization at the applied magnetic field of 100 Oe. The ferromagnetic ordering in the nanorods has a Curie temperature of ~37 K, different from that of MnO at around 25 K,[49, 50] and similar with previous Mn-doped ZnO 1D nanostructures.[51, 52] Surprisingly, the doped ZnO nanocrystalline bowls and cages presented ferromagnetic behavior above room temperature after subtracting the diamagnetic contribution from the silicon substrate, as shown in Figure 4.6 (b), where the inset shows the as-collected data from SQUID measurement. The corresponding coercivity field and saturation magnetization of the Mn-doped ZnO bowls/cages are 77 Oe and 0.005 emu /g, respectively. The ferromagnetism observed in the as-synthesized Mn-doped ZnO nanostructures may attribute to the substitution of isovalence Mn ions in Zn cations. A stronger magnetization in nanorods was observed at 5K compared to that in the bowls and cages, which possibly resulted from higher Mn concentration in ZnO

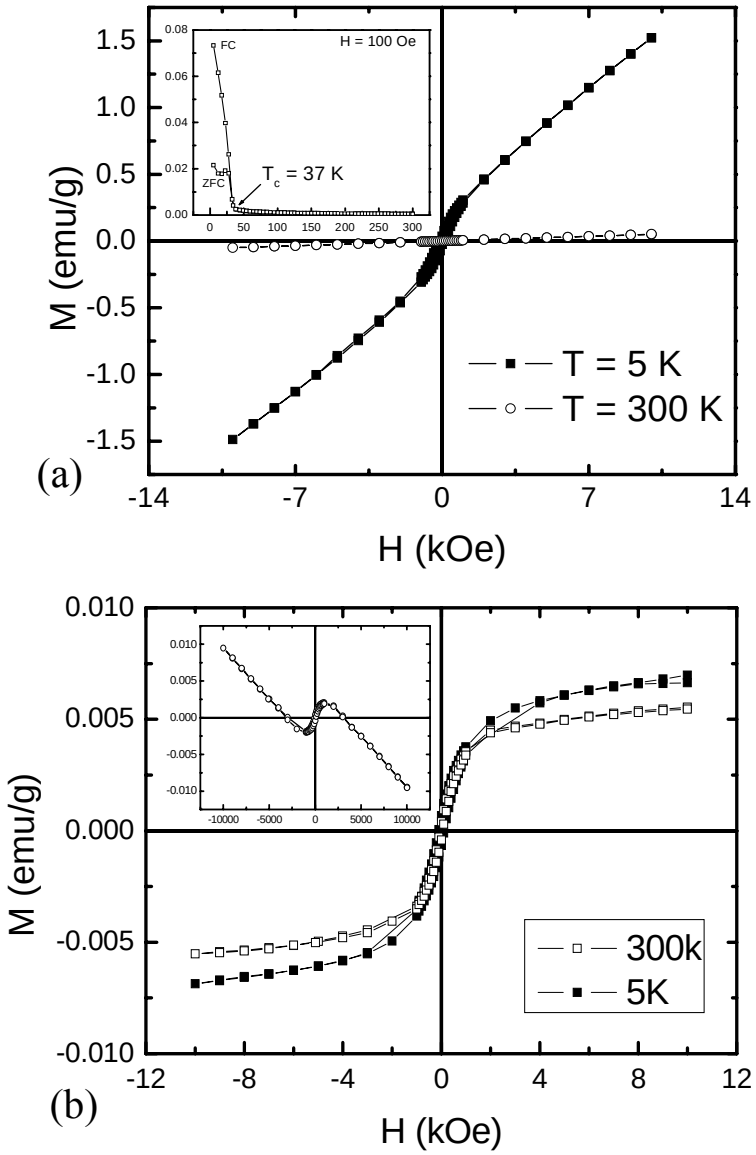

Figure 4.6 (a) Magnetization as a function of magnetic field for the as-grown $Zn_{9.98}Mn_{0.02}O$ nanorods at 5 K, showing low-temperature ferromganetic ordering. The inset is magnetization as a function of temperature, revealing the Curie temperature is about 37 K. (b) Hysteresis loops of the nanocrystalline Mn-doped ZnO bowls/cages after subtracting the diamagnetic contribution from the Si substrate. The inset is the as-collected data from SQUID measurement.

nanorods grown *in situ* than that in bowls and cages deposited at lower temperature regions. One possible reason could be that the ferromagnetic coupling induced by the overlap of unoccupied 3*d* states with impurity band such as oxygen vacancies[53-55] is

favored at lower temperature deposition zones, where a large amount of defects were formed.

4.2 Approach II

4.2.1 Morphology

The FESEM images of sample 7-3-I, 8-3-I and 9-3-I obtained *in situ* in our CVD reactor through approach II at different temperature are shown in Figure 4.7. Again, distinctive features were observed upon different synthesizing temperature. Figure 4.7 (a) and (b) are side-view and top-view images of sample 7-3-I grown at 750ºC. ZnO islands are distributed on a polycrystalline ZnO surfaces at relatively low density. Each island is about 1 μm tall and 400 nm in diameter, processing a hexagonal cross section. Figure 4.7 (c) shows well-aligned nanowires with uniform diameter, length, and density grown perpendicularly on a bulk crystalline substrate. The nanowires have a smooth surface and no catalyst cap was found at the tips, as shown in the enlarged image in Figure 4.7 (d). The dimensions of the nanowires are about 100 nm in diameter and 15 μm long. The as-fabricated nanowire arrays have great potential in spintronic nanodevice application. Sample 9-3-I grown at 950 ºC also demonstrated well-aligned nanorods, but with a lower aspect ratio. As shown in Figure 4.7 (e) and the enlarged top view image (f), the nanorod arrays are about 200nm in diameter and over 2 μm long with an obvious hexagonal cross section. It is clearly shown that growing temperature has great influence on the morphology of ZnO nanostructures. At relatively low reaction temperature of 750ºC,

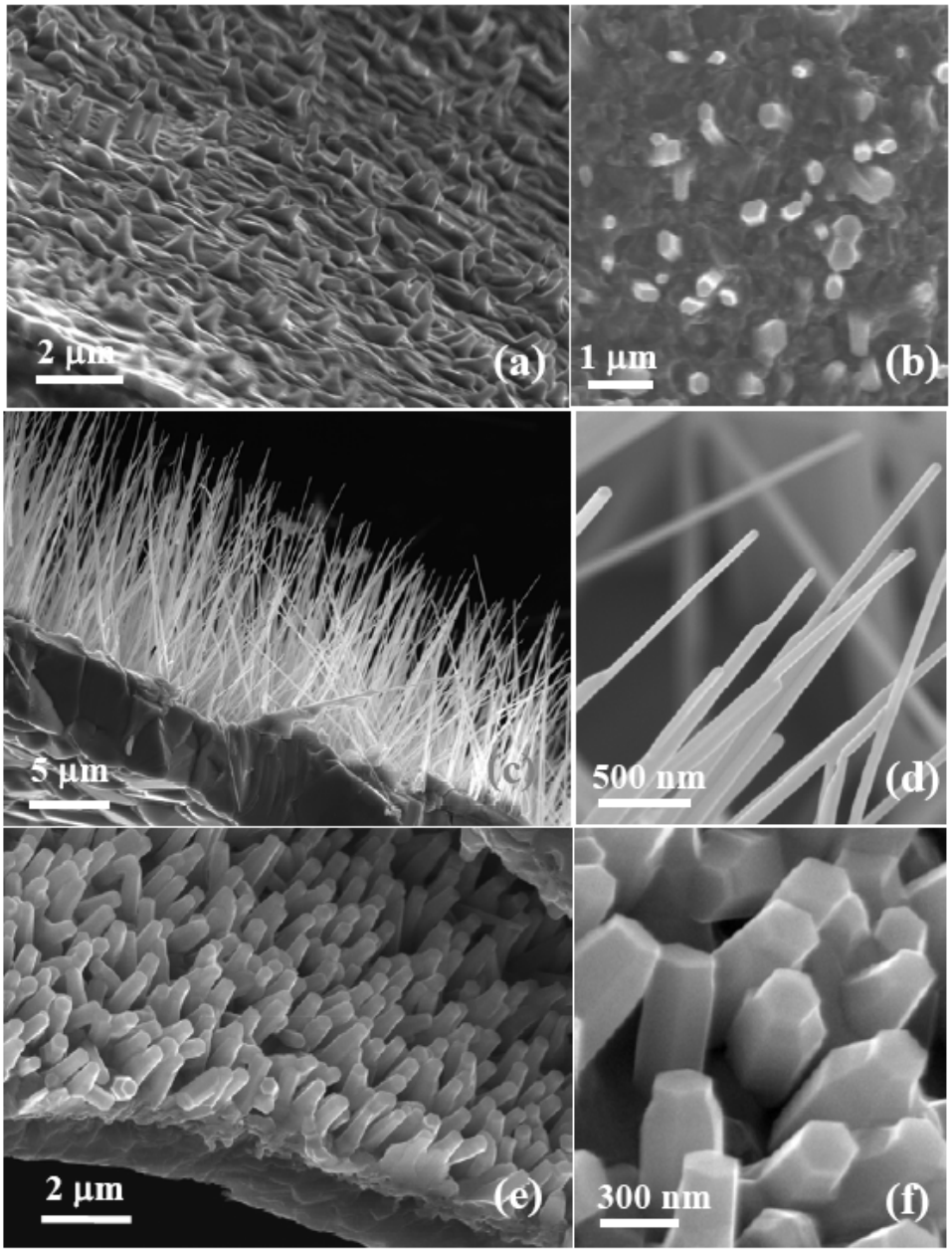

Figure 4.7 (a), (c), (e) and corresponding enlarged picture (b), (d), (f) are FESEM images of sample 7-3-I, 8-3-I and 9-3-I synthesized at 750ºC, 850ºC, and 950ºC respectively.

inhomogeneous growth of nanowires was observed on a polycrystalline ZnO substrate. One reason might be that the temperature couldn't provide enough energy for ZnO crystal to overcome the surface potential and grow out one dimensionally. When

temperature was set at 850ºC, optimum conditions were achieved for well-aligned nanowire growth in our CVD system. The initial Zn/ZnO droplets formed at the melting points of Zn are considered the catalysts for the vapor-liquid-solid (VLS) growth of the well-aligned Mn doped ZnO nanowires.[56] Zn foil played an very important role in the synthesis. In addition to be Zn source of the CVD reaction, the foil also acts as a framework for the formation of well-aligned nanowire arrays.[56] As temperature goes higher to 950 ºC, ZnO crystal is kinetically favorable to grow faster in higher energy facet along *a* axis instead of *c* axis, resulting in thicker nanorod arrays with much smaller aspect ratio.

4.2.2 Structure Analysis

Closer investigation was performed on a single nanowire of sample 8-3-I by TEM and the results are illustrated in Figure 4.8. No catalyst and nanocluster were observed on

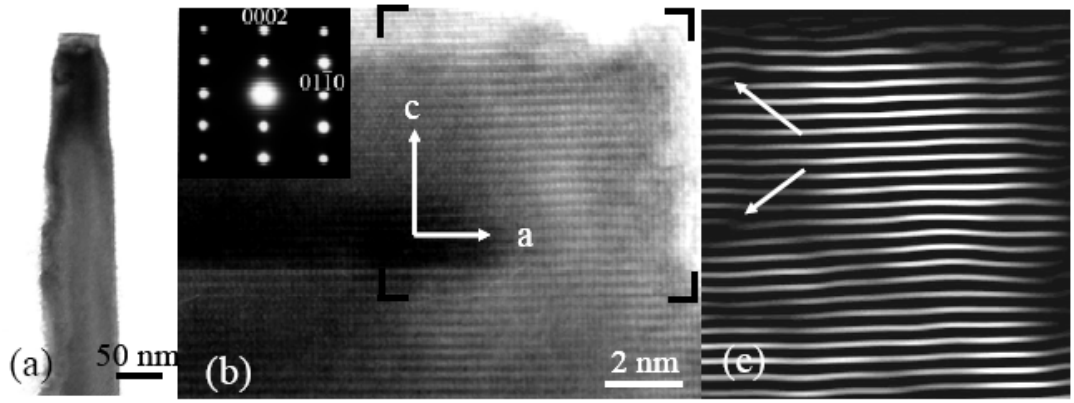

Figure 4.8 (a) TEM image of a single 8-3-I nanowire. (b) A lattice image of the single crystalline $Zn_{1-x}Mn_xO$ nanowire and the inset is SADP of nanowires, showing *c*-axis growth. (c) The back and forth fast Fourier transformation (FFT) analysis using the 000 ± 1 diffraction spots, showing stacking faults and lattice deformation denoted by arrows

the nanowire tip and surface from Figure 4.8(a). The lattice fringe image of circled region in Figure 4.8(b) and the corresponding SADP in the inset, reveal that the nanowires are single crystalline ZnO wurtzite structure possessing a growth direction along the *c* axis, which is coincident with the hexagonal cross section of FESEM iamges. Similiar results were obtained for ZnO well-aligned nanowires grown by other groups.[57, 58] back and forth fast Fourier transformation (FFT) analysis was used for the lattice image bracketed inside the rectangle region in Figure 4.8(b), using the 000±1 diffraction spots. Stacking faults (denoted by arrows) and lattice deformation were clearly observed in Figure 4.8(c), which could be attributed to the substitution of larger Mn cations into the Zn sites in ZnO lattice. TEM investigation was also performed on sample 7-3-I and 9-3-I. Morphology information consistent with their corresponding FESEM images was found. All the 1-D nanoarrays are determined as wurtzite structure with *c-axis* preferential growth.

Figure 4.9 shows the powder diffraction XRD patterns of the as-prepared 1-D nanostructure arrays, revealing comprehensive phase and structure information in addition to TEM results. First of all, all of the three patterns demonstrate sharp peaks correspond to standard ZnO x-ray powder diffraction pattern, suggesting samples grown under 750ºC, 850 ºC and 950 ºC are well crystallized, consistent with TEM single crystalline features. For sample 8-3-I and sample 9-3-I, (002) peak prevails than the usually most intensively diffraction peak, (101) peak, obviously revealing the c-axis preferential growth of the well-aligned nanowires and nanorods determined by SADP analysis previously. Peaks from other ZnO crystal plans are considered attributing to the

polycrystalline ZnO substrate, from which the 1-D nanostrustures are grown. Obvious shift of ZnO peaks towards smaller diffraction angle was observed in sample 7-3-I, 8-3-I, and 9-3-I, indicating an increase of ZnO lattice distance with higher grown temperature.

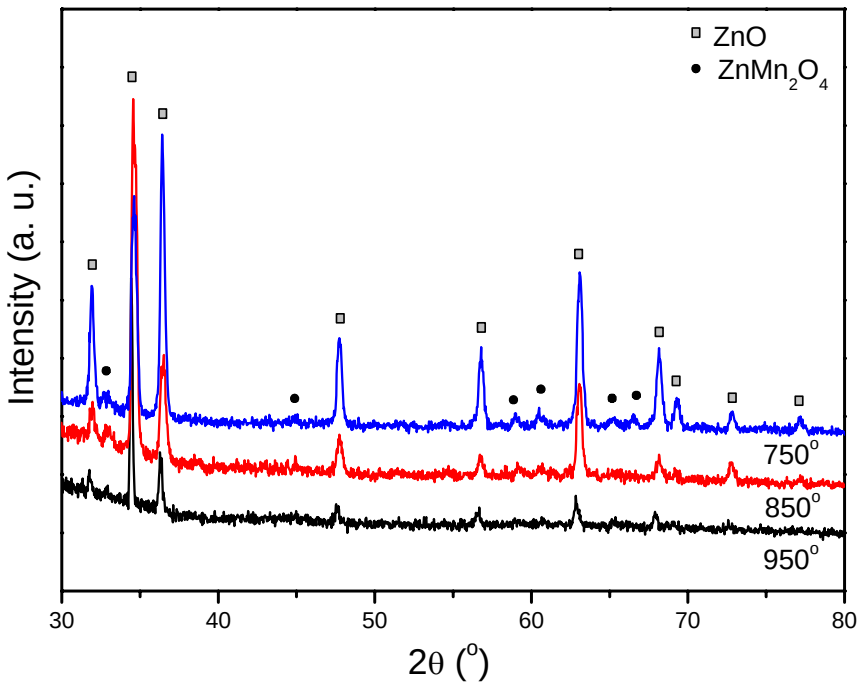

Figure 4.9 XRD patterns of sample 7-3-I, 8-3-I, and 9-3-I grown in approach II at 750ºC, 850 ºC, and 950 ºC respectively.

The enlargement of ZnO lattice distance might attribute to more Mn substitution of Zn cations, since Mn^{2+} has large ionic radius than Zn^{2+}. Signals corresponding to a second phase, hetaerolite ($ZnMn_2O_4$), were found in sample 7-3-I and, although very weak, in sample 8-3-I as well. Despite of the large solubility of Mn in ZnO lattice, segregation of second phase has been reported by many groups studying DMS $Zn_{1-x}Mn_xO$ system[59, 60] and is considered origin of ferromagnetism. The formation of $ZnMn_2O_4$ in our experiments hasn't been reported before. As shown in Figure 4.9, the proportion of

$ZnMn_2O_4$ in sample 8-3-I is much lower than that of sample 7-3-I, suggesting phase segregation tends to exist at lower temperature for a rather short deposition time duration. While at higher synthesizing temperature, 950ºC, no trace of second phase was detected by XRD diffraction.

To investigate Mn distribution, EDS point scan was performed *in situ* in FESEM for sample 7-3-I, 8-3-I, and 9-3-I fabricated at 750ºC, 850ºC, and 950ºC respectively. Typical EDS spectra for three samples are shown in Figure 4.10. Besides C peak arising from carbon tape on the SEM stub, Zn and O peaks, as well as Mn peak are evident in the spectra. As far as the Mn peak intensity is concerned, sample 7-3-I fabricated at 750ºC in approach II appears to have higher Mn concentration than the well-aligned nanowires and nanorods grown at 850ºC, and 950ºC. The Mn atomic ratio in ZnO nanostructures was estimated to be about 9%, 1.7%, and 2% for sample 7-3-I, 8-3-I, and 9-3-I respectively. Since vapor phase reactions are subjected to Mn loss by sublimation at high temperature[61], we suggest that for a relatively low fabrication temperature 750ºC, Mn tends to retained in-situ of tube furnace forming a second phase of hetaerolite $ZnMn_2O_4$. When temperature goes higher to 950 ºC, both the sublimation and diffusion rate of Mn increase, resulting in less Mn concentration in ZnO matrix but more homogeneous distribution (sample 9-3-I). Therefore, it is understandable that sample 8-3-I synthesized at a moderate temperature of 850 ºC with medium Mn sublimation and diffusion, has slightly lower Mn concentration than that of 9-3-I and very weak trace of $ZnMn_2O_4$ indicated by XRD pattern (Figure 4.9).

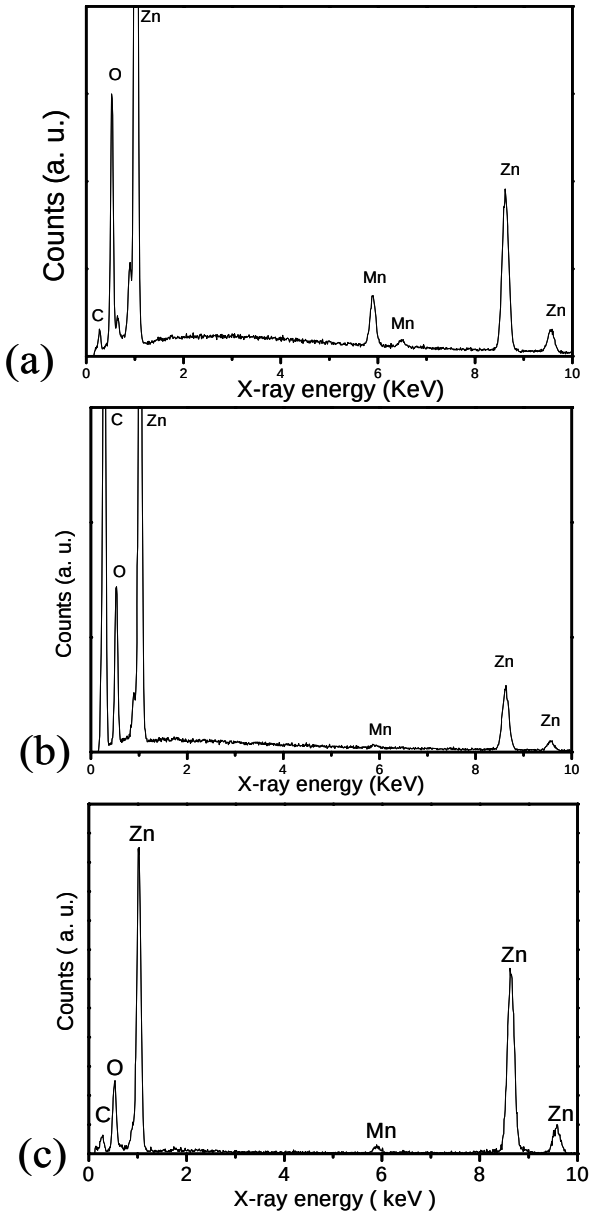

Figure 4.10 EDS spectra of the well-aligned $Zn_{1-x}Mn_xO$ nanostructures. Mn peak is clearly observed. (a) sample 7-3-I, (b) sample 8-3-I, (c) sample 9-3-I

4.2.3 Magnetic Properties

Figure 4.11 shows the magnetization as a function of applied magnetic field for sample 7-3-I, 8-3-I, and 9-3-I measured by SQUID at 5k and 300K. The diamagnetic

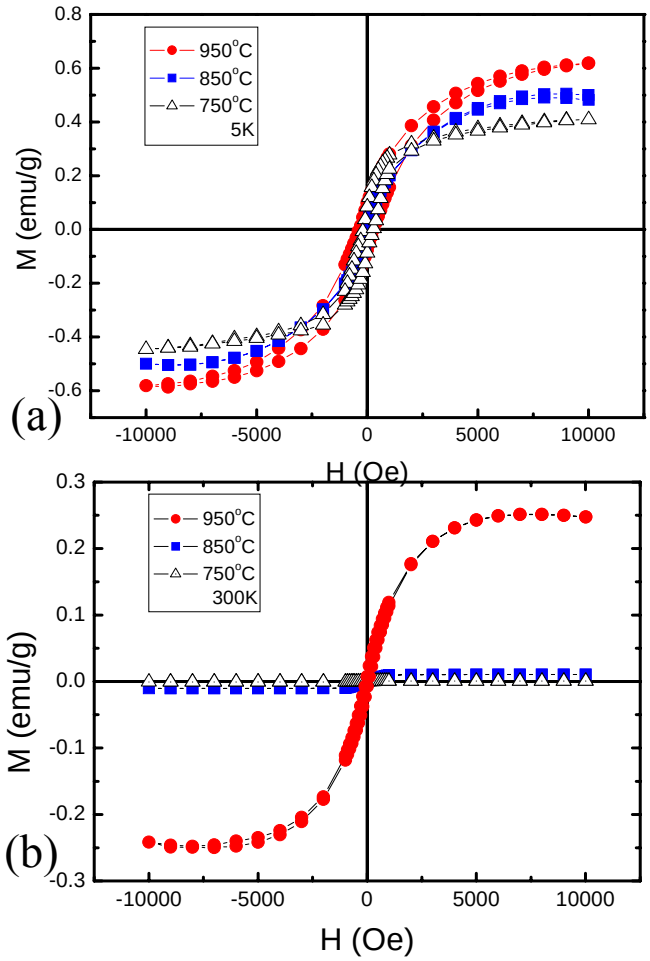

Figure 4.11 (a) and (b) Magnetization as a function of magnetic field for the as-grown well-aligned nanorods, nanowires, and nano islands at 5K and 300K, respectively.

background of the Teflon tape has been subtracted. Hysteresis loops of well-aligned nano islands, nanowires, and nanorods show both low-temperature and room-temperature ferromagnetic behavior. Opposite with previous observation of room-temperature ferromagnetism in low-temperature processed Mn doped ZnO thin films[59] and well-aligned nanowires[62], ferromagnetic ordering was enhanced at high fabrication temperature. Sample 9-3-I, well-aligned nanorods grown at 950ºC, has the largest

saturation magnetization (M_s) among three samples measured at both 5K and 300K, with values of 0.6 emu/g and 0.25 emu/g, respectively. As shown in Figure 4.11 (a), saturation magnetization of the as-synthesized nanowire arrays (sample 8-3-I) and nano islands (sample 7-3-I) at 5K are 0.53 emu/g and 0.39 emu/g respectively. However, as illustrated in figure 4.11 (b), the values of M_s of both sample 8-3-I and 7-3-I decreased drastically above room temperature, estimated as 0.01 emu/g and 7×10^{-4} emu/g respectively. Even though, the lowest M_s values from our CVD process are two orders of magnitude higher than the reported ~10^{-6} emu for Mn doped ZnO nanowires at room temperature.[62] The origin of ferromagnetism in Mn doped ZnO has been under persistent debate over years. Many earlier studies of Mn^{2+}:ZnO revealed only paramagnetism, or at best ferromagnetism below room temperature, with T_C ranging from 37 to 250 K.[63-65] It is not until very recently was ferromagnetism above room temperature reported for Mn^{2+}:ZnO,[4, 62] but with low saturation moments indicative of only partial magnetic ordering. Still, several laboratories have claimed to observe ferromagnetism arising only from phase segregated impurities and not from the DMSs themselves.[59, 66] In our experiments, despite the segregation of a nonmagnetic phase: hetaerolite ($ZnMn_2O_4$) at lower processing temperature 750ºC-850 ºC, room-temperature ferromagnetic ordering was still observed in the as-fabricated well-aligned 1-D nanostructures. In high-temperature processed sample 9-3-I, well-aligned ZnO nanorods with more Mn substitution indicated by XRD study, has much stronger ferromagnetic interaction above 300K. The room-temperature ferromagnetic phase couldn't be Mn-related oxides such as MnO, MnO_2,

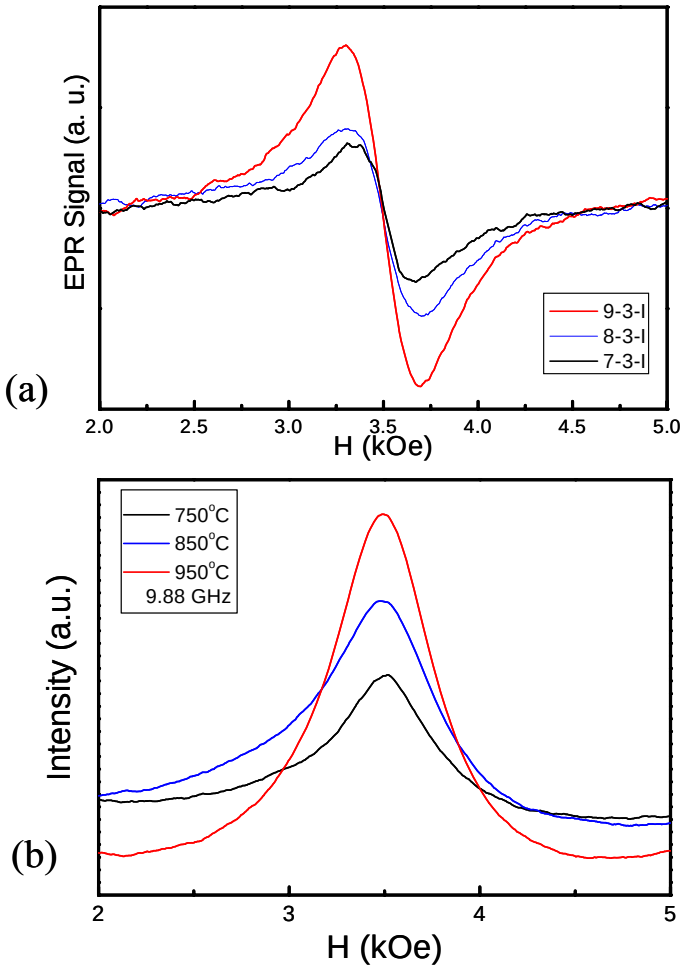

Figure 4.12 (a) FMR spectra and (b) integrated curves of sample 7-3-I. 8-3-I. and 9-3-I measured bv EPR at 300K

Mn_2O_3 and Mn_3O_4, because none of them shows ferromagnetism above room-temperature. The T_C of Mn_3O_4 is around 43K, lower than room temperature; MnO, MnO_2, and Mn_2O_3 are antiferromagnetic material with Neel temperature of 116, 84, and 80K. The Mn^{2+}: ZnO model are favorable to high temperature ferromagnetic ordering by electron doping of Zn intersitials[67] and the overlap of 3d state with donor impurity band of oxygen vacancy[55]. Along with the XRD analysis, we can conclude that the room temperature ferromagnetism arise from the isovalent Mn^{2+} substitution of Zn cations in

the as-fabricated ZnO nanostrucures. At higher synthesizing temperature 950 ºC, more substitution of Zn cations by Mn^{2+} could take place, resulting in much higher saturation magnetization than nanowires and islands grown at 750 ºC and 850 ºC, respectively, where less Mn is substituted in ZnO lattice and a second phase of $ZnMn_2O_4$ is segregated.

Figure 4.12 shows the room temperature EPR results for the as-obtained sample 9-3-I (well-aligned nanorods), 8-3-I (well-aligned nanowires), and 7-3-I (nanoislands). Broadened Lorenzian single lines at about g = 2.00 are observed for all samples. This broad feature, a so-called ferromagnetic resonance (FMR) signal,[68] arises from transitions within the ground state of a ferromagnetic domain. No six-feature hyperfine lines of nuclear magnetic hyperfine coupling for Mn^{2+} (I=5/2) was observed in Figure 4. 12 (a), resembling there's no paramagnetic Mn^{2+} related phase in our samples[4, 69]. From integrated curves in Figure 4.12 (b), it is clearly shown that the overall ferromagnetic interaction for sample 9-3-I (well-aligned nanorods grown at 950ºC) is much stronger than that of sample 8-3-I and 7-3-I, consistent with the saturated magnetization results from SQUID measurement.

4.3 Approach III

4.3.1 Morphology and Structure

Figure 4.13 are the FESEM images of sample 8-3-IA, 8-3-IB, and 8-3-IC processed at 850ºC in approach III. Consistent with approach II, well-aligned nanowires with uniform diameter, length, and density grown perpendicularly on a bulk crystalline

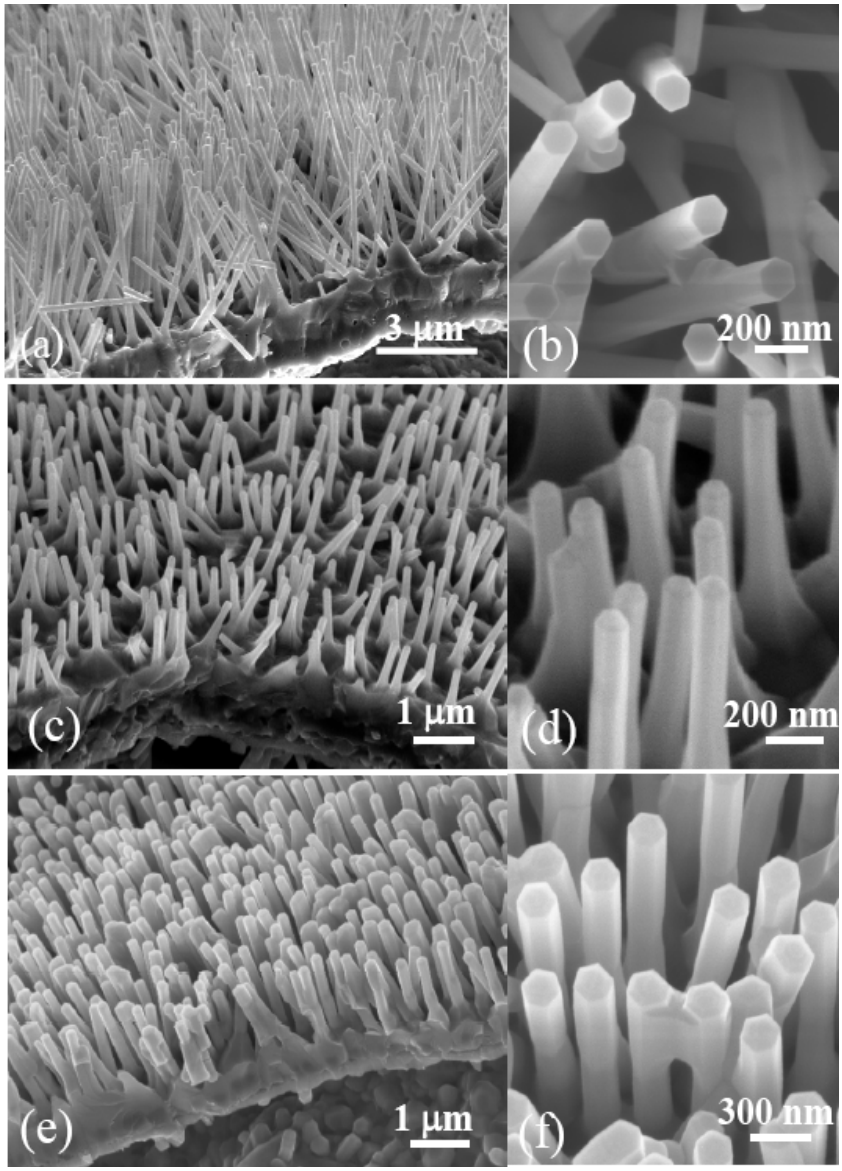

Figure 4.13 FESEM images of as-prepared well-aligned nanowires through approach III. (a) and (b) sample 8-3-IA with nominal Mn concentration of 5 at.%, (c) and (d) sample 8-3-IB with nominal Mn concentration of 10 at.%, (e) and (f) sample 8-3-IC with nominal Mn concentration of 15 at.%

substrate are achieved for each sample. The nanowires have a smooth surface and no catalyst cap was found at their tips. Slightly morphology differences are observed for nanowires with different Mn doping ratio. Figure 4.13 (a) and (b) are side-view and enlarged top-view images of Sample 8-3-IA with a nominal Mn concentration of 5 at.%.

The nanowires with largest aspect ratio are fabricated at this doping ratio, with dimensions about 5 μm long and 100 nm in diameter. Sample 8-3-IB (10at.% Mn) has shorter nanowires with lower density on the substrate, comparing with sample 8-3-IA (5at.% Mn), as shown in Figure 4.13 (c) and (d). The dimensions of the nanowires are about 200 nm in diameter and 2 μm long. At nominal Mn concentration of 15 at.%, sample 8-3-IC are well-aligned nanowires with the smallest aspect ratio (about 2 μm long 200 nm in diameter) as demonstrated in Figure 4. 13 (e) and (f). The length of the nanowires fabricated in approach III is much smaller than those grown in approach II. The Zn foil is placed perpendicular to the air flowing direction in reaction configuration of approach III, in order to create more contact opportunity between O_2 molecules with Zn source. However, in this geometry the growing direction of nanowires is opposite to the gas flowing, which to some extent suppressed the nanowires growth. Figure 4.13 indicates that the aspect ratio of the as-synthesized well-aligned $Zn_{1-x}Mn_xO$ nanowires decreased with increasing of Mn concentration. The EDS spectrum of sample 8-3-IA, 8-3-IB, and 8-3-IC with 5 at.%, 10 at.%, and 15 at.% Mn added are shown in Figure 4.14 (a), (b), and (c) respectively. Same trend of Mn concentration with the nominal doping rate was observed in the well-aligned nanowires. The atomic concentration of Mn in sample 8-3-Ia, 8-3-IB, and 8-3-IC were estimated to be 1.3%, 2.5%, and 5%, smaller than the corresponding nominal doping rate, which might caused by sublimation of Mn at the high reaction temperature 850ºC. Figure 4.15 shows the XRD patterns of as-synthesis well-aligned nanowires with different Mn doping rate. Peaks corresponding to strong

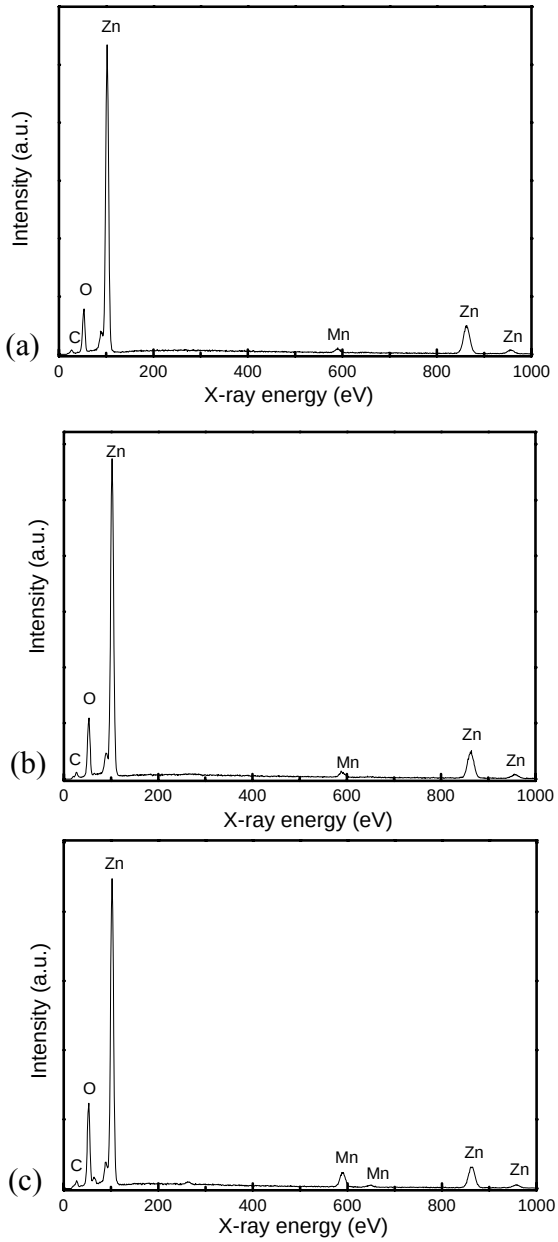

Figure 4.14 EDX spectrum of sample 8-3-IA, 8-3-IB, and 8-3-IC of nominal 5 at.%, 10at.% and 15at.% Mn doping.

diffraction of wurtzite ZnO and weak diffraction of hetaerolite $ZnMn_2O_4$ were clearly observed for sample 8-3-IA, 8-3-IB, and 8-3-IC fabricated in approach III. Sharp peaks of ZnO with a prevailing (002) diffraction peak indicate highly crystalline ZnO with preferential growth along c-axis. As shown in the enlarged XRD pattern in inset of Figure

4.15, an evident shift toward smaller diffraction angle (left shift) was observed as the Mn doping ratio increased, revealing more Mn^{2+} ions are substituted in ZnO lattice with the increase of nominal Mn concentration. Comparing with approach II, larger amount of

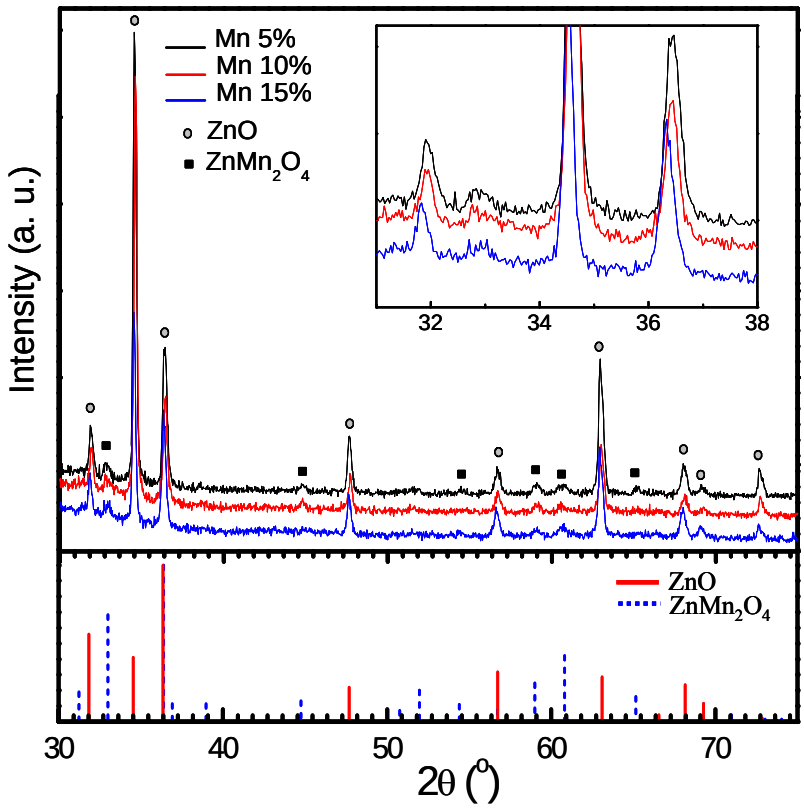

Fingure 4.15 XRD pattern of well-aligned Mn doped ZnO nanowires synthesized in approach III. Inset shows the enlarge diffraction pattern.

second phase (hetaerolite $ZnMn_2O_4$) were detected by XRD at reaction temperature of 850ºC, which might attribute to the perpendicular reaction configuration (referring Figure 3.5) obscuring Mn sublimation.

Figure 4.16 (a), (b) and (c) are the Zn *2p,* O *1s*, and Mn *2p* XPS high resolution spectra of the as-prepared ZnO nanowires with 15 at.% nominal Mn doping. Strong peaks at 1022.65 eV and 1044.85 eV were observed for Zn 2p scanning (Figure 4.16 (a)), which

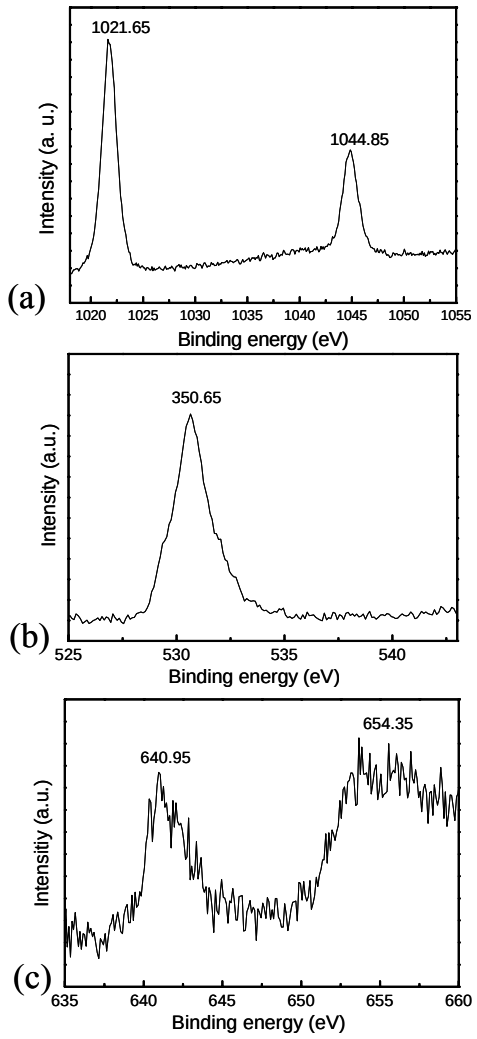

Figure 4.16 XPS spectra of well-aligned nanowires with 10 at.% Mn doping (sample 8-3-IC). (a) Zn 2p (b) O 1s (c) Mn 2p.

are in agreement with the binding energies of Zn $2p_{3/2}$ and Zn $2p_{1/2}$, respectively. The narrow line widths of Zn 2p peaks indicate that the binding energy of Zn^{2+} are predominated in the sample and the influence of Mn is negligible.[60] From Figure 4.16 (c), two broad peaks appear at 640.95 eV and 654.35 eV, revealing the existence of of Mn^{2+}. The quantity analysis shows that the Mn concentration on the nanowire surface is 3.4

at.%, smaller than the EDS estimation of ~5 at.%, which might implies Mn^{2+} ions are deeply doped into the nanowires instead of diffused on the surface.

4.3.2 Magnetic properties Studies

Figure 4.17 shows the magnetization as a function of applied magnetic field at 5k and 300K for the three samples synthesized in approach III. The diamagnetic background of the Teflon tape has been subtracted. Both low-temperature and room-temperature ferromagnetism are obvious in the heteresis loops for all samples fabricated by approach III. The saturation magnetization of the as-grown nanowire arrays with nominal 5 at.%, 10 at.%, and 15 at.% Mn doping are 0.79 emu/g, 2.12 emu/g, and 0.55 emu/g respectively at 5K. At room-temperature, the value of M_s for sample 8-3-IA, 8-3-IB, and 8-3-IC are 0.002 emu/g, 0.017 emu/g, and 9.34×10^{-4} emu/g. Sample 8-3-IB with 10% nominal Mn doping and experimental Mn concentration of 2.5 at.% (estimated by EDS) has strongest ferromagnetic interaction among three samples, both at low temperature and room-temperature. Since the second phase $ZnMn_2O_4$ is nonmagnetic, it is suggested that the room-temperature ferromagnetism caused by the substitutional dopinig to Mn^{2+} in ZnO lattice. When Mn concentration in ZnO lattice is too high, those Mn^{2+} ions which stay within the distance of direct *3d-3d* interaction will exhibit antiferromagnetic coupling. Thus has negative contribution to the overall ferromagnetism, resulting in lower M_s observed in sample 8-3-IC with 15 at.% nominal Mn concentration. Sample 8-3-IA with 5 at% nominal Mn doping ratio has the lowest M_s, indicating a weak ferromagnetic coupling by less Mn doping.

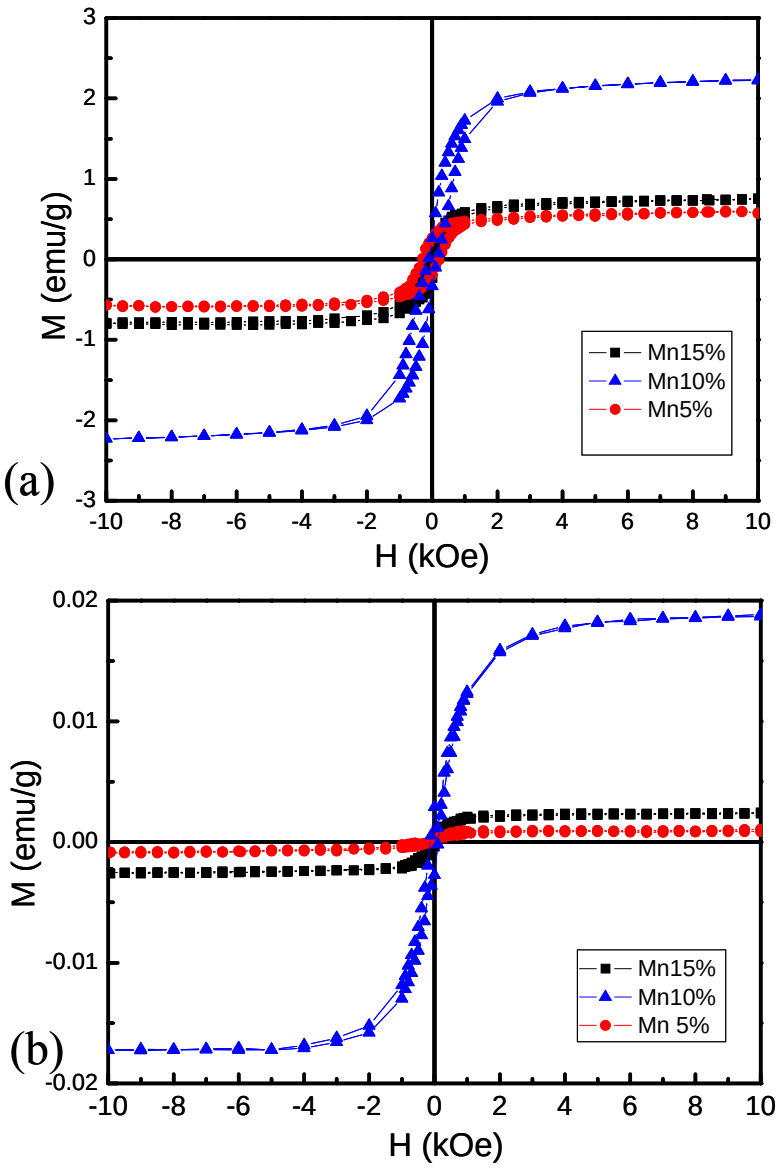

Figure 4.17 magnetization as a function of applied magnetic field curve for the well-aligned nanowires with 5 at.%, 10 at%, and 15 at.% nominal Mn doping grown in approach III (a) at 5K, (b) at 300K.

CHAPTER 5

CONCLUSION

Well-aligned DMS $Zn_{1-x}Mn_xO$ nanowire and nanorod arrays were successfully synthesized *in-situ* from metallic Zn foil and $MnCl_2 \cdot 6H_2O$ under air flow at 850ºC-950 ºC using a chemical vapor deposition method. Employment of Zn foil as start material provides the frame for the formation of well-aligned nanowire arrays. The as-grown nanowires and naorods are single crystalline wurtzite structure and possess a growth direction along the *c* axis. By the same methods, low-dimensional nanostructures such as bowls and cages were fabricated from powder mixture of Zn and $MnCl_2 \cdot 6H_2O$ on (001) Si surface at the downstream side of tube furnace with substrate temperature of 450 ºC-550 ºC.

Synthesizing temperature has a great influence on the morphology, chemical composition, and the resulting magnetic properties of the as-formed DMS nanowire and nanorod arrays. 850 ºC is considered the most optimistic temperature for ZnO crystal growth, at which nanowires with highest aspect ratio were obtained. In terms of doping and ferromagnetic interaction, however, higher synthesizing temperature is favored. At 950ºC, Mn^{2+} ions are substituted into ZnO lattice with atomic concentration of 2%, resulting in room-temperature ferromagnetism with saturation magnetization of 0.25 emu/g. On the other hand, at lower synthesizing temperatures (750 ºC and 850 ºC), segregation of a nonmagnetic second phase-hetaerolite ($ZnMn_2O_4$) appears, which in turn

reduced the Mn^{2+} substituted in ZnO lattice, causing weaker room-temperature ferromagnetic coupling than samples obtained at 950 ºC. As far as Mn concentration is concerned, nanowires with nominal 10at.% Mn doping ratio have strongest ferromagnetic coupling. The intensity of magnetic coupling increase with Mn doping ratio until a critical point, the anitferromagnetic coupling of direct interaction between Mn^{2+} ions will subtract the overall ferromagnetic in DMS system.

Reference

[1] H. Ohno, *Science* **281** (14), 951 1998

[2] S. Takeyama and R. R. Galazka, *Phys. Status Solidi* (b) **96** (1), 413 (1979)

[3] P. kacman, *Semicond. Sci. Technol.* **16** (4), R25 (2001)

[4] P. Sharma, A. Gupta, K. V. Rao, F. J. Owens, R. Sharma, R. Ahuja, J. M. Osorio Guillen, B. Johansson, G. A. Gehring, *Nature Mater.* **2**, 673 (2003)

[5] T. Dietl, H. Ohno, F. Matsukura, J. Cibert, D. Ferrand, *Sience*, **287**, 1019 (2000)

[6] T. Fukumura, Z. Jin, M. Kawasaki T. Shono and T. Hasegawa, S. Koshihara, H. Koinuma, *Appl. Phy. Lett.* **78**, 958 (2001)

[7] S. Jung, S. J. An, G.-C. Yi, C. U. Jung, S.-I. Lee, S. Cho, *Appl. Phy. Lett.* **80**, 4561 (2002)

[8] M. H. Kane, K. Shalini, C. J. Summers, R. Varatharajan, J. Nause, C. R. Vestal, Z. J. Zhang, and I. T. Ferguson, *J. of Appl. Phy.* **97**, 023906 (2005)

[9] A. Tiwari, C. Jin, A. Kvit, D. Kumar, J. F. Muth and J. Narayan, *Solid State Commn*. **121**, 371 (2002)

[10] Zhengwu Jin, T. Fukumura, M. Kawasaki, K. Ando, H. Saito, T. Sekiguchi, Y. Z. Yoo, M. Murakami, Y. Matsumoto, T. Hasegawa, and H. Koinuma, *Appl. Phy. Lett.* **78**, 3824 (2001)

[11] J. K. Furdyna, *J. of Appl. Phy.* **64** (4) R29, 1988

[12] J. Spalek, A. Lewicki, Z. Tarnawski, J. K. Furndyna, R.R. Galazka, Z. Obuszko, *Physical Review B* **33** (5), 3407 (1986)

[13] K. C. Hass and H. Ehrenreich, J. Cryst. Growth **86**, 8 (1988)

[14] K. Sato and H. Katayama-Yoshida, *Semicond. Sci. and Technol*. **17**, 367 (2002)

[15] H. Ikada, T. Saito, N. Takahashi, K. Shibata, T. Sato, Z. Chen, I. Souma, and Y. Oka, *Physica E (Amsterdam)* **10**, 373 (2001)

[16] L. Chen, P. J. Klar, W. Heimbrodt, F. Brieler, M. Froobab, H.-A. Krug von Nidda, and A. Loidl, *Physica E (Amsterdam)* **10**, 368 (2001).

[17] J.J. Wu, S. C. Liu, M. H. Yang, *Appl. Phys. Lett.* **85**, 1027 (2004)

[18] C. Ronning, P. X. Gao, Y. Ding, and Z. L. Wang, *Appl. Phys. Lett.* **84**(5), 783 (2004)

[19] C. Geng, Y. Jiang, Y. Yao, X. Meng, J. A. Zapien, C. S. Lee, Y. Lifshitz, and S. T. Lee, *Adv. Funct. Mater.* **14**, 589 (2004)

[20] M. Jaczynski, J. Kossut, and R.R. Galazka, *Phys. Status Solidi b* **88**, 73 (1978)

[21] H. Liu, *Phys. Rev.* **121**, 451 (1961)

[22] J. R. Schrieffer and P. Wolf, *Phys. Rev.* **149**, 491 (1966)

[23] J.R. Schrieffer, *J. Appl. Phys.* **38**, 1143 (1967)

[24] A. K. Bhattacharjee, G. Fishman, and B. Coqblin, *Physca B, C* **117-8**, 449 (1983)

[25] M. Arciszewska and M. Nawrocki, *Phys. Chem. Solids*, **47**, 309 (1986)

[26] M. Nawrocki, F. Hamdani, J. P. Lascaray, Z. Golacki, and J. Deportes, *Solid State Commun.* **77**, 111 (1991)

[27] R. K. Zheng, H. Liu, X.X. Zhang, V. A. L. Roy, A.B. Djurisic, *Appl. Phys. Lett.* **85**, 2589 (2004)

[28] J. Blinowski, P. Kacman, *Acta Phys. Polon.* **84**, 693 (1993)

[29] B.E. Larson, K. C. Hass, H. Ehrenreich, and A.E. Carlsson, *Phys. Rev.* B **37B**, 4137 (1988)

[30] B.E. Larson and H. Ehrenreich, *Phys. Rev.* B **39**, 1273 (1989)

[31] G. Bastard, and C. Lewiner, *Phys. Rev.* B **20**, 4256 (1979)

[32] C. Zener, *Phys. Rev.* **82**, 403 (1951)

[33] P. W. Anderson and H. Hasegawa, *Phys. Rev.* **100**, 675 (1955)

[34] K. Sato and H. Katayama-Yoshida, *Japan J. Appl. Phys.* **39**, L555 (2000)

[35] G. A. Medvedkin, T. Ishibashi, T. Nishi, K. Hayata, Y. Hasegawa, and K. Sato *Japan. J. Appl. Phys.* **39,** L949 (2000)

[36] J. Blinowski and P. Kacman, *Acta Phys. Polon.* **90** 731 (1996)

[37] H. J. M. Swagten, W. J. M. deJonge, R. R. Gałazka, P. Warmenbol and J. T. Devreese *Phys. Rev.* B **37** 9907 (1988)

[38] T. Story, P. J. T. Eggenkamp, C. H. W. Swuste, H. J. M. Swagten, W.J.M. deJonge and L.F. Lemmens, *Phys. Rev.* B **45** 1660 (1992)

[39] T. Dietl, A. Haury and Y. Merle d'Aubign´e, *Phys. Rev.* B **55** R3347 (1997)

[40] T. Dietl, J. Cibert, D. Ferrand and Y. Me.rle d'Aubig´e, *Mater. Sci. Eng.* B **63** 103 (1999)

[41] D. Ferrand, J. Cibert,a) A. Wasiela, C. Bourgognon, S. Tatarenko, G. Fishman, S. Koles´nik, J. Jaroszyn´ ski, T. Dietl, B. Barbara, and D. Dufeu, *J. Appl. Phys.* **87** 6451 (2000)

[42] Y. Q. Chang, D. B. Wang, X. H. Luo, X. Y. Xu, X. H. Chen, L. Li, C. P. Chen, R. M. Wang, J. Xu, and D. P. Yu, *Appl. Phys. Lett.* **84** (19) 4020 (2003)

[43] J. J. Liu, M. H. Yu, and W. L. Zhou, *J. Appl. Phys.* **99**, 08M119-1 (2006)

[44] R. S. Wagner and W. C. Ellis, Appl. Phys. Lett. **4**, 89 (1964).

[45] L. Wang, X. Zhang, S. Zhou, Y. Zhou, and J. Qi, Appl. Phys. Lett. **86**, 024108 (2005).

[46] P. X. Gao and Z. L. Wang, *J. Am. Chem. Soc.* **125**, 11299 (2003).

[47] H. P. Sun and X. Q. Pan, *J. Mater. Res.* **19**, 3062 (2004).

[48] X. Y. Kong, Y. Ding, and Z. L. Wang, *J. Phys. Chem.* B **108**, 570 (2004).

[49] G. H. Lee, S. H. Huh, J. W. Jeong, J. C. Choi, S. H. Kim, and H.-C. Ri, *J. Am. Chem. Soc.* **124**, 12094 (2002).

[50] W. S. Seo, H. H. Jo, K. Lee, B. Kim, S. J. Oh, and J. T. Park, *Angew. Chem.*, Int. Ed. **43**, 1115 (2004)

[51] Y. Q. Change *et al.*, *Appl. Phys. Lett.* **83**, 4020 (2003).

[52] S. W. Jung, S. J. An, and G. C. Yi, *Appl. Phys. Lett*. **80**, 4561 (2002).

[53] A. Punnoose, J. Hays, A. Thurber, M. H. Engelhard, R. K. Kukkadapu, C.Wang, V. Shutthanandan, and S. Thevuthasan, *Phys. Rev.* B **72**, 054402 (2005)

[54] J. M. D. Coey, A. P. Douvalis, C. B. Fitzgerald, and M. Venkatesan, *Appl. Phys. Lett.* **84**, 1332 (2004)

[55] M. Venkatesan, C. B. Fitzgerald, J. G. Lunney, and J. M. D. Coey, *Phys. Rev. Lett.* **93**, 177206 (2004)

[56] J.J. Liu, M.H. Yu, and W.L. Zhou, *Appl. Phys. Lett.* **87**, 172505 (2005)

[57] M. H. Zhao, Z. L. Wang, and S. X. Mao, *Nano Lett.* **4**, 587 (2004)

[58] W. I. Park, G.-C. Yi, M. Kim, and S. J. Pennycook, *Adv. Mater.* **14**, 1841 (2002)

[59] D. C. Kundaliya, S. B. Ogale, S.E. Lofland, S. Dhar, C.J. Metting, S. R. Shinge, Z. Ma, B. Varughese, K.V. Ramanujachary, L. Salamanca-Riba, and T. Venkatesan, *Nature Mater.* **3** 709 (2004)

[60] L.W. Yang, X.L. Wu, G.S. Huang, T. Qiu, and Y.M. Yang, *J. Appl. Phys.* **97,** 014308 (2005)

[61] V. A. L. Roy, A. B. Djurisic, H. Liu, X. X. Zhang, Y. H. Leung, M. H. Xie, J. Gao, H. F. Lui, and C. Surya, *Appl. Phys. Lett.* **84**, 756 (2004)

[62] J. M. Baik and J.L Lee, *Adv. Mater.* **17**, 2745 (2005)

[63] T. Fukumura, Z. Jin, A. Ohtomo, H. Koinuma, M. Kawasaki, *Appl. Phys. Lett.* **75**, 3366 (1999).

[64] K. Ueda, H. Tabata, T. Kawai, *Appl. Phys. Lett.* **79**, 988 (2001),

[65] D. P. Norton, S. J. Pearton, A. F. Hebard, N. Theodoropoulou, L. A. Boatner, R. G. Wilson, *Appl. Phys. Lett.* **82**, 239 (2003)

[66] Park, J. H.; Kim, M. G.; Jang, H. M.; Ryu, S.; Kim, Y. M. *Appl. Phys. Lett.* **84**, 1338 (2004)

[67] M. H. F. Sluiter, Y. Kawazoe, P. Sharma, A. Inoue, A. R. Raju, C. Rout, and U.V. Waghmare, *Phys. Rev. Lett.* **94,** 187204 (2005)

[68] Y. Sasaki, X. Liu, and J. K. Furdyna, M. Palczewska, J. Szczytko, and A. Twardowski, *J. Appl. Phys.* **91**, 7484 (2002)

[69] M. Diaconu, H. Schmidt, A. Pöppl, R. Böttcher, J. Hoentsch, A. Klunker, D. Spemann, H. Hochmuth, M. Lorenz, and M. Grundmann, *Phys. Rev. B* **72**, 085214 (2005)

Vita

Jingjing Liu was born February 21, 1982 in Dujiangyan city, China. In June 2002 she received her Bachelor's Degree in Materials Science and Engineering from Southwest Jiaotong University with esteemed honor. In June, 2005, she received her Master's Degree in the same institute. She is going to receive her M. S. in Physics from the University of New Orleans in August 2006.